BEAM-SCANNING REFLECTARRAY ENABLED BY FLUIDIC NETWORKS

A Dissertation

by

STEPHEN ANDREW LONG

Submitted to the Office of Graduate Studies of
Texas A&M University
in partial fulfillment of the requirements for the degree of

DOCTOR OF PHILOSOPHY

December 2011

Major Subject: Electrical Engineering

BEAM-SCANNING REFLECTARRAY ENABLED BY FLUIDIC NETWORKS

A Dissertation

by

STEPHEN ANDREW LONG

Submitted to the Office of Graduate Studies of
Texas A&M University
in partial fulfillment of the requirements for the degree of

DOCTOR OF PHILOSOPHY

Approved by:

Chair of Committee,	Gregory H. Huff
Committee Members,	Robert D. Nevels
	H. Rusty Harris
	Laszlo B. Kish
Head of Department,	Costas N. Georghiades

December 2011

Major Subject: Electrical Engineering

ABSTRACT

Beam-Scanning Reflectarray Enabled by Fluidic Networks. (December 2011)

Stephen Andrew Long, B.S.; M.S., Texas A&M University

Chair of Advisory Committee: Dr. Gregory Huff

This work presents the design, theory, and measurement of a phase-reconfigurable reflectarray (RA) element for beamforming applications enabled by fluidic networks and colloidal dispersions. The element is a linearly polarized microstrip patch antenna loaded with a Coaxial Stub Microfluidic Impedance Transformer (COSMIX). Specifically, adjusting the concentration of highly dielectric particulate in the dispersion provides localized permittivity manipulation within the COSMIX. This results in variable impedance load on the patch and ultimately continuous, low-loss phase control of a signal reflected from the patch. Different aspects of design, modeling, and measurement are discussed for a proof-of-concept prototype and three further iterations.

Initial measurements with manual injections of materials into a fabricated proof-of-concept demonstrate up to 200° of phase shift and a return loss of less than 1.2 dB at the operating frequency of 3 GHz. The next design iteration addresses fabrication challenges as well the general cumbersomeness of the proof-of-concept by replacing the static material delivery system with a dynamic closed-loop fluidic network. It also makes use of a design procedure to maximize the phase sensitivity. Measurements demonstrate

progressive phase shifts through dilution of the system reservoir; however, the initial measurements with this system are not in line with simulated predictions. Investigations suggest the primary culprit to be inaccurate material data. The dielectric constant of the particulate (colloidal BSTO) was overrated and the loss tangent of the fluid medium (a silicone-based oil) was underrated. After accounting for these issues the measurement a second measurement with the system demonstrates 270° of phase shift with return loss of 9 dB. The next design iteration examines a trade-off between phase sensitivity and reduced losses. The design also features modifications to the fluidic system to allow for layered fabrication in the GND plane as well integration with a 2-port coaxial measurement cell. Attempted measurements discover the fluidic system cannot flow the higher concentrations of nanoparticles necessary for phase shifting. A final design iteration addresses this challenge by expanding and repositioning inlets to the fluidic system. Free space reflection measurements with this element initially demonstrate phase shifting until a buildup of nanoparticles form within the COSMIX.

NOMENCLATURE

RL	Return Loss
Rx	Receiver
Tx	Transmitter
RA	Reflectarray
BSTO	Barium Strontium Titanate
VSWR	Voltage Standing Wave Ratio
PDMS	Polydimethylsiloxane
LC	Liquid Crystal
AF	Array Factor
SMA	SubMiniature Version A
RWG	Rectangular Waveguide
TEM	Transverse Electromagnetic
W.R.T.	With Respect To

TABLE OF CONTENTS

LIST OF FIGURES

LIST OF TABLES

CHAPTER I

INTRODUCTION

Many directed energy (DE) applications such as radar, long distance communication, or weapons including the Active Denial System (ADS) require the use of high-gain antennas in order to operate effectively. Often the antenna of choice is the familiar parabolic reflector. Though conceptually simple, this antenna lacks the ability to scan (sweep) its direction of focus without the aid of a mechanical rotation, and even then the speed and angles of the scan are limited. The phased array represents one alternative - a typically planar grid-like arrangement of small antennas equipped with individually controllable phase-shifters - which can electronically scan energy to wide angles. However, the phase-shifters for these arrays are not only expensive but present additional losses to the input signal, requiring the system to use additional amplifiers. Reflectarray (RA) antennas, on the other hand, offer both the feeding efficiency of conventional shaped reflector antennas along with the planar form and beam-pointing capabilities of microstrip phased arrays [1]. However, the various integrated mechanisms which provide the beam-pointing ability require the design engineer to make trade-offs between weight, power consumption, scan resolution, complexity, and cost [2]. Topologies in the literature feature devices such as PIN diodes [3], MEMS [4], ferroelectric thick films [5], liquid crystal [6, 7], and many other architectures derived from phased array techniques. As diverse as these technologies are, they uniformly

_____

This thesis follows the style of *IEEE Transactions on Antennas and Propagation.*

require bias circuitry integrated on or in the antenna element itself. In some cases this can lead to design challenges, fabrication difficulties, and potentially significant losses in the reflected signal. Recent developments in dynamic material systems [8-10] have expanded the design space for reconfigurable RF devices and antennas to include microfluidic networks.

This dissertation begins by introducing the important mechanisms and concepts that form the foundation for understanding the RA design; a sampling of current technologies available for reconfiguring RA elements provides additional background and motivation for the approach used in this work. The theory and operation of the mechanisms aid in understanding the design rationale behind the RA unit cell. The RA unit cell progresses through four design iterations before it expands into a 1 x 5 array. Simulated models validate the theoretical considerations as well as the designs. Currently available materials and fabrication methods provide measured results that demonstrate successful phase shift but highlight future needs for electromagnetically functional materials. A summary concludes the work.

CHAPTER II

BACKGROUND

A. *Reflectarray Antennas*

As mentioned previously the RA antenna represents a hybrid between the familiar reflector and the phased array. A phased array is a general term for a wide range of systems, but this work refers to a particular subset involving microstrip technology. Fig. 1 illustrates the operation of a phased array. A single feed (in this case a microstrip line) branches out via power dividers to every element within the array. An independently controlled, surface-mounted phase-shifter and amplifier feeds every element. The electronically controlled phase-shifters allow for very fast (μs) steering of the beam of the array. The rectangular grid of microstrip dipoles gives the entire structure the fabrication benefit of piecewise planar form.
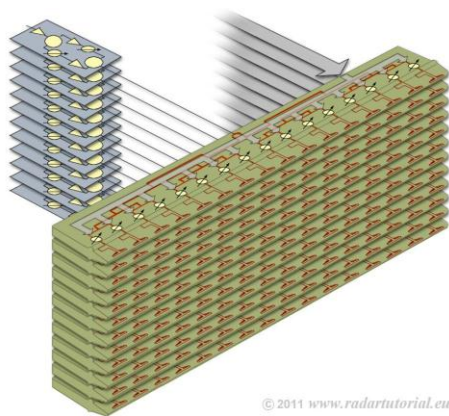
Fig. 1. Layout of a piecewise planar phased array

There are several trade-offs to consider. First, the elements themselves, as well as the phase distribution required for a desired scan angle, are very frequency dependent. The beam direction will tilt as the operating frequency shifts, even if the phase-shifters and other active devices provide consistent, frequency-independent phase modulation. Also the efficiency and power-handling capabilities of planar feed networks are limited. Power dissipates as a result of dielectric and metallization losses. For the larger arrays required in high gain applications, this can lead to losses of 3dB (50%) or more. Phased arrays often require liquid cooling systems to manage the heat from this dissipated power as well as from the power consumed in the electronic devices across the array. Also, the active devices built into the unit cells generate heat and non-linearities in received/transmitted signals.

Fig. 2 illustrates operation of the parabolic reflector antenna using ray tracing. The curved surface of the reflector collimates the reflected rays, giving the aperture focus in the broadside direction. This (theoretically) frequency-independent feature suggests the reflector may have infinite bandwidth, provided the radiation patterns of the feed antenna are also frequency-independent. Also, the air between the feed and the reflector dissipates very little power. However, manufacturing the curved surface is difficult for higher frequencies of operation (smaller tolerances) and for small scale applications. Mounting a curved reflector on superstructures presents a greater challenge than mounting a flat reflector. The parabolic reflector antenna relies upon on external mechanisms to provide rotation in order to redirect the focus of its energy. Those

systems introduce additional weight, and the scan speed and angles are much more limited compared to a phased array.
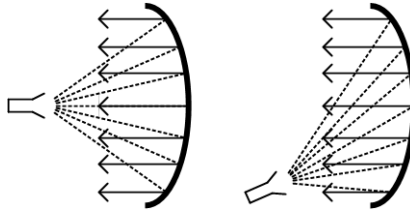
Fig. 2. Parabolic reflector principle

The reflectarray combines the feeding efficiency of the reflector antenna with the electronic scanning capability and planar form of the microstrip phased array. The reflectarray illustrated in Fig. 3 operates by illuminating a panel of reflector antennas. Each reflector antenna receives and reradiates the incident signal with a specific magnitude and time delay (phase) determined by its orientation to the feeding antenna (more on this in the following sections). The aperture as a whole lacks focus because every element reradiates with a different phase, leading to destructive interference. The integration of phase-loading mechanisms on each element provides compensation for these phase differences such that the reradiated signals *constructively* interfere in a certain direction (providing focus). A beam-steering RA features dynamic, in-situ control of all the loading mechanisms. This degree of control allows the reradiated signals constructively interfere and form a beam in a new direction. Note that the antenna itself remains fixed. This process depicted in Fig. 3 (right) the beam redirecting process, which requires no mechanical rotation, and is referred to as *electronic beam-*

steering. Switching speed, losses, and phase resolution of the loading mechanisms remain critical metrics of performance just as they are with a phased array.
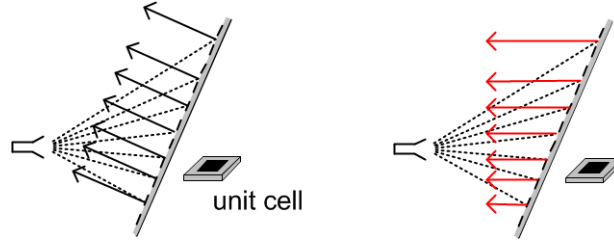
Fig. 3. Planar reflectarray focusing at broadside (left) and refocusing off broadside (right)

B. *Microstrip Antennas*

The unit cell depicted in Fig. 3 is a microstrip patch antenna. Microstrip antennas consist of substrate materials clad with one or more layers of metal. Current lithography methods allow fast and cost-effective fabrication of many designs. Basic designs have a single substrate layer of height *h* with metal on both sides. In the case of a microstrip patch antenna, the top layer is patterned to form a metal rectangle with a length *L* and width *W*. The cavity formed between the two metal layers has an electromagnetic resonance that allows the antenna to efficiently transmit or receive power radiated from other antennas. Boundary conditions established by the conductive faces of the volume (top and bottom) and nonconductive faces (the four open side-walls) setup the field distribution in the cavity (see Fig. 4). The effective length, $L_{eff} = L + 2\Delta L,$ of the microstrip patch antenna determines the resonant frequency f_0 for the dominant mode.

This parameter accounts for the length *L*, the material properties of the substrate ε_{rs}, and the length extensions $2\Delta L$ from the fringing fields at the edges of the patch. The effective relative permittivity ε_{reff} of the substrate material determines the effective wavelength λ_{eff} according to Eq. (1). From (1), increasing the permittivity of a region increases the number of wavelengths inside, making the region "electrically longer." This allows engineers to design small antennas that resonate at lower frequencies.
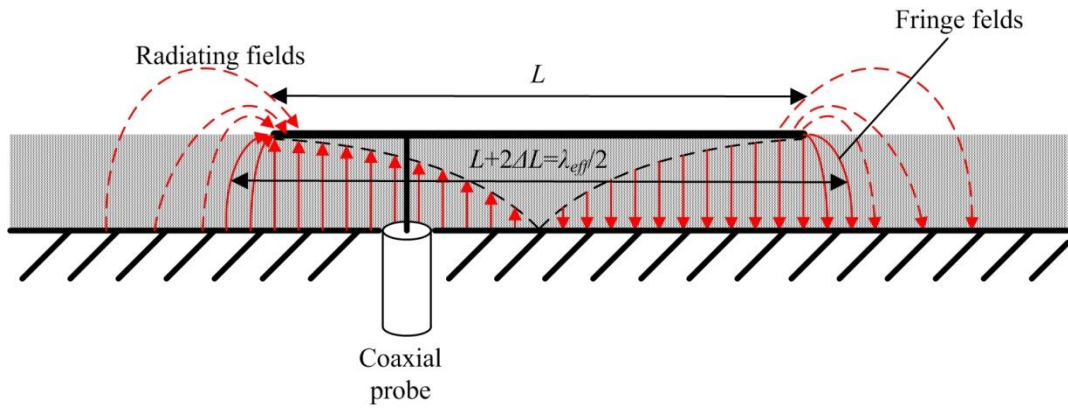
Fig. 4. The TM_{10} electric fields of the microstrip patch antenna

$$\lambda_{eff} = \frac{\lambda_0}{\sqrt{\varepsilon_{reff}}} = \frac{c/f}{\sqrt{\varepsilon_{reff}}} \tag{1}$$

Fig. 4 illustrates the patch antenna's fundamental (resonant) mode - the TM_{10} mode - which has maximum amplitude of the electric field at both edges and a half-period distribution in between. The fields at these edges are out of phase by 180º (see the reversed direction of the vertical electric field lines) and extend from the edges of the antenna, becoming the *fringing fields*. The fringe fields extend outward from the patch,

decreasing in strength and become the *radiated fields*. The radiating edges at either side of the antenna (separated by the length dimension) are often referred to as *slots*. The 180º phase relationship and the effective distance L_{eff} between these slots determine the radiation pattern of the antenna. A coaxial line can deliver energy into the patch via a coaxial probe. The position of a coaxial probe relative to the length of the patch determines the coupling between the patch and the coax line.

C. *Impedance and Reflection*

Measurement of the voltage and current at the input terminals of an antenna determines the input impedance Z_A according to (2). In the general case this complex number is expressed in terms of *resistance* and *reactance*, the real and imaginary components respectively. The impedance of an antenna (and most devices) varies as a function of frequency and where the terminals are in contact with the antenna and its ground plane.

$$Z_A(f) = \frac{V_A(f)}{I_A(f)} = \frac{|V_A(f)| \angle \varphi_V^\circ}{|I_A(f)| \angle \varphi_I^\circ} = \text{Re}(Z_A(f)) + j\,\text{Im}(Z_A(f)) \tag{2}$$

The impedance of an antenna determines how much power from a transmission line or other media will couple into or reflect from an antenna. The transmission line has a characteristic impedance Z_0 (typically 50 Ω). A mismatch between the impedances results in reflection at the junction according to (3). The input reflection coefficient S_{11} characterizes this reflection and features magnitude and phase.

$$S_{11} = \frac{Z_A - Z_o}{Z_A + Z_o} = \mathrm{Re}(S_{11}) + j\,\mathrm{Im}(S_{11}) = |S_{11}|e^{j\theta} \qquad (3)$$

$$|S_{11}|^2 = \frac{\text{Reflected Power}}{\text{Input Power}} \qquad (4)$$

A coefficient of $|S_{11}| = 0$ indicates zero reflected power and $|S_{11}| = 1$ (or 0 dB) indicates total reflection. This work aspires to design and measure a reflective element. Thus, a greater S_{11} indicates better performance. The designed element should also demonstrate the ability to manipulate the phase θ by as much as 360°.

D. *Current Microstrip RA Technology*

Many topologies in the literature [2] provide *dynamic* phase compensation of microstrip antennas in a reflectarray. This work organizes these technologies into two categories, switch-based and material based systems. The former operates with n-bit discrete phases. These topologies typically load the radiator with a segmented transmission line (Fig. 5) with an effective length controlled by turning certain combinations of switches on and off. Different effective line lengths result in different electrical delays in the reflected signal. The switches may be active devices such as PIN diodes, but more recent publications have focused on the use of MEMS [4, 11-14].
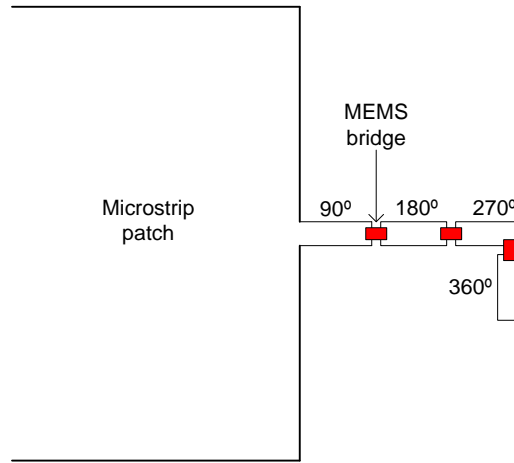
Fig. 5. MEMS controlled 2-bit reconfigurable RA element

Though MEMS could provide continuous phase control if operated as a varactor, recent works in the literature focus on their use as switches. MEMS provide μs switching speeds, high quality factors, and consume little or no power. However, implementing MEMS can be a serious challenge in design since engineers need to know and account for their equivalent circuit parameters. Furthermore MEMS are limited in power-handling capabilities, require substantial voltages to operate, and may require additional feedback mechanisms to detect MEMS stiction (a state of being permanently in the "down" position). Fig. 6 depicts two examples of MEMS based phase-shifters used in tunable RA unit cells. The design on the left couples incident energy from the patch into a microstrip line via a slot in the patch. An RF MEMS switch controls the electrical length of that line in a 1-bit manner (i.e. a two-state switch). The design on the right operates similarly by coupling incident energy in from a vertical slot and then making that energy take one of four different paths out to be reradiated by a horizontal slot. The

paths are determined by which RF MEMS (shown as red squares) are active. This design offers 2-bit phase control.
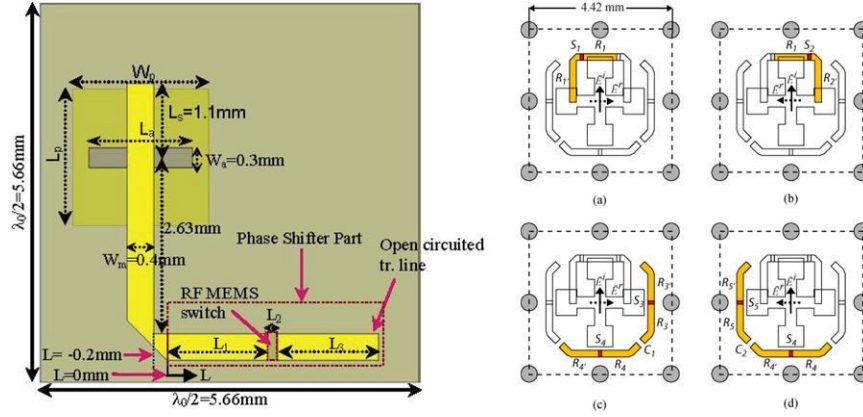
Fig. 6. MEMS-operated RA elements

Switch-based topologies in general face an issue of phase resolution due to the nature of n-bit operation. Work by the author (shown later in the theory section) as well as work in [15] determined that, as a rule of thumb, 3-bit phase resolution (i.e. 45°) provides sufficient gain for most applications. However, this rule assumes all the possible phases are spread out evenly. A design in [16] proves how difficult that is to achieve as even a 5-bit MEMS switchable RA element shows 45° (3-bit resolution) gaps in its phase curve. While simply increasing the number of states (switches) in a RA element may solve the phase resolution problem, it does so at increased cost and complexity.

Analog, continuously-tunable reconfiguration mechanisms provide a viable alternative to switch-based topologies. Specifically, approaches involving material perturbation have

shown promise in [5-7]. Local permittivity manipulation in the RA element via a bias voltage changes the electrical load of the element. The work in [5] achieves this by etching the antenna metallization upon a thick-film BST (a ferroelectric) layer and bisecting the element to create a variable-capacitive gap. The designs in [6, 7, 17] back the element with a liquid-crystal (LC) cavity (Fig. 7). An applied bias voltage tilts the molecular alignment in the LC, altering the effective permittivity of the LC, and thereby adjusting the electrical load from the cavity. Fig. 6 illustrates both these techniques.
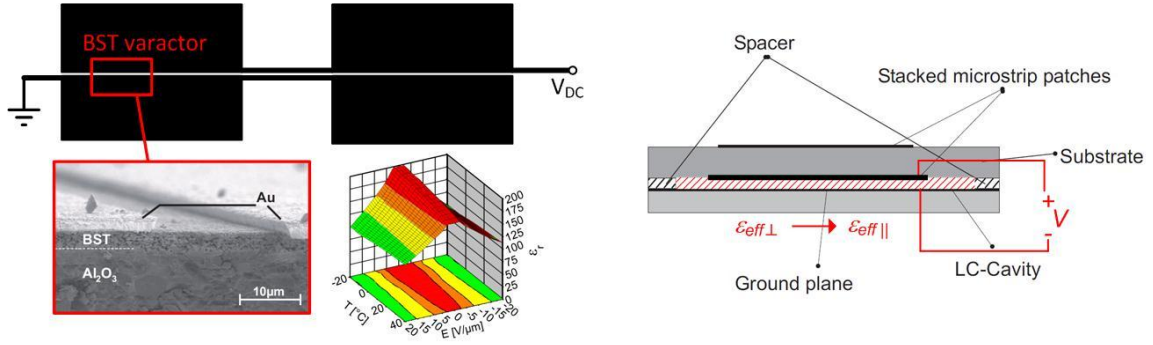
Fig. 7. RA elements using ferroelectric materials

CHAPTER III

THEORY

A. Model of Reflectarray

i. Phased Array Theory

Some basic principles aid in understanding the importance of phase manipulation and its role in scanning the beam of an array. Fig. 8 compares the electric fields radiated from an isotropic element and an array. Each element radiates an omnidirectional pattern (i.e. the signal strength is uniform for any angle from the element). An array of these elements produces an aggregate pattern referred to as the *array factor (AF)*. As an example, consider a uniformly spaced ($d = \lambda_o/2$), uniformly excited ($A_m = 1$, $\beta_m = 0$), linear array of $M = 5$ elements. The *AF* of Eq. (5) sums up the contribution of all elements in this array for a given angle from the array ψ.

Isotropic radiator   5-element array

Scanned to 30°
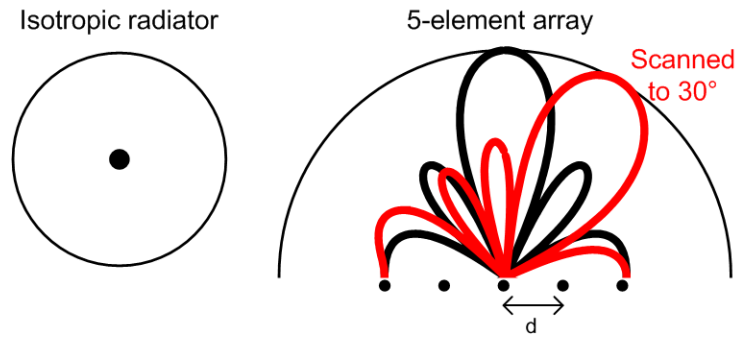
Fig. 8. The field pattern of an isotropic radiator (left) and a 5-element array (right)

$$AF(\psi) = \sum_{m=1}^{M} A_m e^{j\beta_m} e^{jkmd\sin\psi} \qquad (5)$$

The plot in Fig. 8 (right) illustrates how the array focuses energy at certain angles where the waves from the elements are in phase (constructive interference). At other angles the waves are out of phase and destructively interfere (i.e. a null). Introducing a progressive phase shift (time delay) of

$$\beta_m = -kmd\sin\psi_0 \tag{6}$$

into how the elements are excited results in the waves coming in phase at a new angle ψ_0 = 30°. The red trace of Fig. 8 (right) reflects this shift. Equation (7) generalizes the expression in (5) for use in a uniformly spaced *rectangular* array in a horizontal coordinate system.

$$AF(\theta_{Az}, \theta_{El}) = \sum_{m=1}^{M}\sum_{n=1}^{N} A_{mn} e^{j\left[k\left(md_x\cos\theta_{El}\sin\theta_{Az} + nd_y\sin\theta_{El}\right) + \beta_{mn}\right]} \tag{7}$$

The angle θ_{Az} is the projection of an observation angle *in* the xz plane an θ_{El} is the observation vector projected *from* the xz plane. Any far-field vector w.r.t. the array can be expressed in terms of θ_{Az} and θ_{El} components in a (similar to expressing in terms of θ and ϕ components). The dimensions d_x and d_y are the element spacing in x and y, respectively. *M* is the number of columns, *N* is the number of rows, A_{mn} represents each element's relative amplitude, and β_{mn} represents the relative phase of each element. In an ideal uniform array

$$A_{mn} = 1 \text{ (uniform)}$$

$$\beta_{mn} = -k\left(md_x \cos\theta_{El0} \sin\theta_{Az0} + nd_y \sin\theta_{El0}\right)$$

where θ_{Az0} and θ_{El0} are the desired angles to focus the array.

ii. *Reflector/Reflectarray Theory*

For a reflectarray A_{mn} will depend on the illumination of each element by the feed antenna (i.e. some elements more brightly illuminated than others) and suffer from losses associated with various the phase-shifting mechanisms (dependence on β_{mn}). Path length differences between the feed and the elements in the array result in different incident phases, and the element phase term β_{mn} must account for this. Chapters in [1] and [18] provide many expressions useful for reflector-based systems, but these expressions typically stem from the following assumptions: 1) the feed is centered about the RA normal vector, 2) the feed radiates a radially symmetric pattern (no φ-dependence) , and 3) the RA itself is circular. Fig 9 (left) illustrates these assumptions.
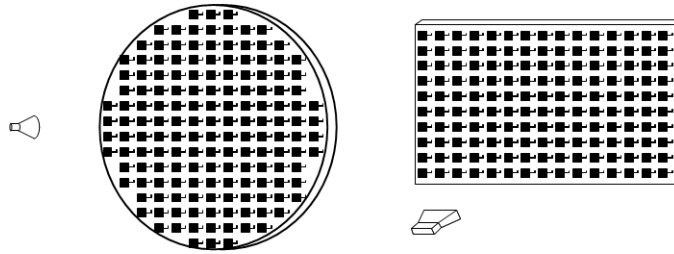
Fig. 9. Circular RA (left) compared with rectangular RA (right)

Expressions based on these assumptions are almost entirely in terms of the spherical angle θ and the *f/d* ratio of the RA. This work analyzes a rectangular RA with a vertically offset feed pointed toward the center of the RA (Fig. 9, right). Expressions in terms of azimuth/elevation coordinates (a.k.a. the horizontal coordinate system) prove more mechanically intuitive than spherical coordinates. The resulting expressions of this work omit the conventional *f/d* parameter since both the focal point and diameter characterize circular geometries and only create ambiguity for rectangular RAs, especially those of substantial aspect ratios.

Accounting for the incident phase and amplitude from the feed upon the elements in the array, the equations for A and β are rewritten as

$$A_{mn} = \underbrace{\left(\cos^{p_{Az}} \theta'_{Az,mn} \cos^{p_{El}} \theta'_{El,mn} \right)}_{F} * \underbrace{\left(\cos^{q_{Az}} \theta''_{Az,mn} \cos^{q_{El}} \theta''_{El,mn} \right)}_{E} \tag{8}$$

$$\beta_{mn} = -\beta_{inc,mn} - k \left(x_{mn} \cos\theta_{El0} \sin\theta_{Az0} + y_{mn} \sin\theta_{El0} \right) \tag{9}$$

where

$$\cos\theta'_{Az,mn} = \cos\theta''_{Az,mn} = \frac{x_{mn} - \overset{0}{x_{feed}}}{z_{feed}} = \frac{x_{mn}}{z_{feed}}$$

$$\theta'_{El,mn} = \cos^{-1}\left(\frac{y_{mn} - y_{feed}}{r_{mn}}\right) - \cos^{-1}\left(\frac{y_{feed}}{z_{feed}}\right)$$

$$\theta''_{El,mn} = \cos^{-1}\left(\frac{y_{mn} - y_{feed}}{r_{mn}}\right)$$

$$r_{mn} = \sqrt{\left(x_{mn} - \overset{0}{x_{feed}}\right)^2 + \left(y_{mn} - y_{feed}\right)^2 + \left(z_{mn} - \overset{0}{z_{feed}}\right)^2} = \sqrt{x_{mn}^2 + \left(y_{mn} - y_{feed}\right)^2 + z_{feed}^2}$$

$$\beta_{inc} = -kr_{mn}$$

and E and F are the field patterns of the element and feed, respectively. The angles θ' and θ'' are taken from the relative coordinates of the feed and element, respectively. The factors p_{Az} and p_{El} characterize the focus of the feed pattern in the azimuth and elevation planes, respectively. A priori measurements of the feed provide these terms. Likewise q_{Az} and q_{El} characterize the element patterns. Multiplying the array factor with the element pattern creates $\mathbf{E}$ the electric field pattern of the RA. Squaring the field pattern provides the power pattern U.

$$\mathbf{E}(\theta_{Az}, \theta_{El}) = AF(\theta_{Az}, \theta_{El}) * E(\theta_{Az}, \theta_{El})$$
$$U(\theta_{Az}, \theta_{El}) = \left|\mathbf{E}(\theta_{Az}, \theta_{El})\right|^2$$

(10)

A broad element pattern (small p) benefits the operation of an RA. A directive element pattern not only reduces the power received from the feed by elements at the edge of the RA (i.e. elements too focused to "see" the feed), but will also attenuate U as the beam is

scanned. For example if $p_{Az} = 1$, then for a scan angle of 45° in the azimuth plane, the AF attenuates U by half.

Spillover efficiency (ε_s) and taper efficiency (ε_t) help determine how well a feed is matched to its reflector. The former characterizes how much of the feed's transmitted power from the feed actually illuminates the reflector. The latter determines how well the reflector utilizes its physical area to provide gain. Fig. 10 illustrates these principles.

ε_s good
ε_t poor

ε_s poor
ε_t good
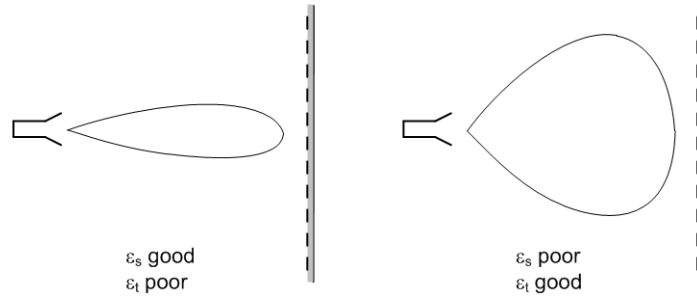
Fig. 10. An RA fed by a highly focused feed (left) and a loosely focused feed (right)

A highly focused antenna feeds the RA in Fig. 10 (left). This focus results in very little energy radiating around the RA, providing a good ε_s. However, the peripheral elements receive relatively little power and hence contribute much less to the gain of the array, so ε_t is poor. This tapered amplitude distribution brings down the potential gain of the array as compared to a uniform array ($A_{mn} = 1$) but provides a positive tradeoff: a tapered aperture has a lower side lobe level (SLL). Side lobes are secondary beams (see Fig. 8, right) and represent unwanted received or transmitted radiation. In contrast, a less focused antenna feeds the RA in Fig. 10 (right). This provides a more even distribution

of energy across the array (good ε_t) but results in more energy spilling over the sides of the RA (low ε_s). This wasted energy has no positive trade off.

Equation (11) provides a means to calculate spillover efficiency. This work assumes the feed radiates in the forward hemisphere only. The numerator on the right represents a simple discrete integration (see Fig. 11) because the surface integral limits for a rectangle in an angular coordinate system are difficult to simplify. For RAs with a small number of elements the accuracy of this method will degrade. However, RAs are typically designed for applications featuring (electrically) large apertures with many elements.

$$\varepsilon_s = \frac{P_{inc}}{P_{rad}} = \frac{\oiint\limits_{array} \left|F\left(\theta_{El},\theta_{Az}\right)\right|^2 d\Omega}{\oiint\limits_{hemisphere} \left|F\left(\theta_{El},\theta_{Az}\right)\right|^2 d\Omega} \approx \frac{\sum\limits_{m=1}^{M}\sum\limits_{n=1}^{N}\left|F\left(\theta'_{El,mn},\theta'_{Az,mn}\right)\right|^2 d\Omega_{mn}}{\int\limits_{\theta_{El}=-\pi/2}^{\pi/2}\int\limits_{\theta_{Az}=-\pi/2}^{\pi/2} \left|F\left(\theta_{El},\theta_{Az}\right)\right|^2 d\Omega} \tag{11}$$

where

$$d\Omega_{mn} = \cos\theta_{El,mn} \cdot d\theta_{El,mn} d\theta_{Az,mn}$$
$$d\theta_{El,mn} = \theta_{El,mn} - \theta_{El,m-1,n-1}$$
$$d\theta_{Az,mn} = \theta_{Az,m} - \theta_{Az,m-1}$$
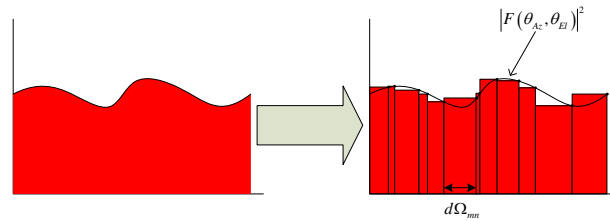
Fig. 11. Illustration of simple numerical integration

Taper efficiency is given below in (12) and stems from (7-223) in [19]. Taper efficiency does not describe dissipated/lost power in the same way spillover does. Rather it represents wasted *real-estate*. Taper efficiency may factor into directivity (and gain) using an effective aperture formula (i.e. (12-37) in [18]). However, calculating directivity through the radiated fields (i.e. (2-23) in [18]) already includes effects of amplitude tapering in the field patterns. Likewise the far-field patterns reflect many other efficiency factors affecting gain. Regardless, taper efficiency remains a useful metric for analyzing the feed antenna and its position.

$$\varepsilon_t = \frac{1}{Area} \frac{\left|\iint A(x,y)\,dxdy\right|^2}{\iint |A(x,y)|^2\,dxdy} = \frac{1}{M \cdot N \cdot d_x \cdot d_y} \frac{\left|\sum_{m=1}^{M}\sum_{n=1}^{N} A_{mn} d_x d_y\right|^2}{\sum_{m=1}^{M}\sum_{n=1}^{N} |A_{mn}|^2 \, d_x d_y} \tag{12}$$

To study the numerical treatment of the RA, this work considers a 15 x 15 array defined by the parameters in Table I. The RA resembles Fig. 9 (right). The feed, the center of the array, and the bottom of the array form an isosceles right triangle with the feed pointed at the center of the RA. Fig.12 shows the incident field amplitude across the RA. The vertical offset of the feed results in a vertically elongated amplitude distribution. The Rx pattern of the elements (i.e. $\cos^q \theta'$) results in additional tapering across the RA. Note that the incident and received amplitude distributions would match if the elements had omnidirectional field patterns ($q = 0$). The incident phase of Fig. 12 (top right) depicts a

spherical wave front originating from the location of the feed. The desired phase distribution in Fig. 12 (bottom right) represents the goal for the phase-shifter network.

Table I

Example design parameters

Parameter	Description	Value
M	Number of columns	15
N	Number of rows	15
dx	Horizontal element spacing	λ/2
dy	Vertical element spacing	λ/2
tilt	Angle feed is offset from RA normal vector	45°
df	Distance between feed and center of RA	(*N*dy*) * sqrt(2)/2
p_{AZ}	Focus factor of feed in azimuth plane	9
p_{EI}	Focus factor of feed in elevation plane	4
q_{AZ}	Focus factor of elements in azimuth plane	0.5
q_{EI}	Focus factor of elements in elevation plane	0.5
θ_{Az0}	Desired scan angle in azimuth plane	30°
θ_{EI0}	Desired scan angle in elevation plane	0°
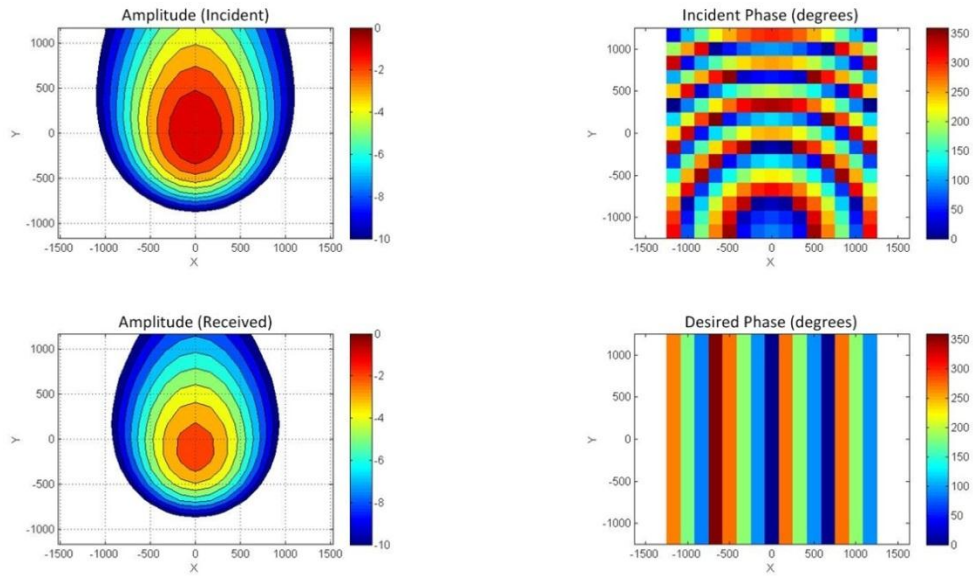
Fig. 12. Offset fed RA of 15 x 15 elements

Fig. 13 shows the impact of phase shifter resolution on the phase across the entire RA. A parameter n rounds off the desired phase correction by $360°/2^n$ increments. Increasing the performance of the phase shifters from 1-bit resolution (180°) to 4-bit resolution (22.5°) allows the RA to better match the desired phase distribution of Fig. 13 (center). The desired phase distribution is uniform w.r.t. the vertical position of the elements and incrementally increases in cycles w.r.t. the horizontal position of the elements. The end result is a beam scanned in the horizontal (azimuth) plane. Phase-shifters with 3-bit resolution create an aperture closely matching the desired phase columns of Fig. 13 (center). Note that despite the color contrast between dark red and dark blue, the two colors represent a (nearly) identical phase.
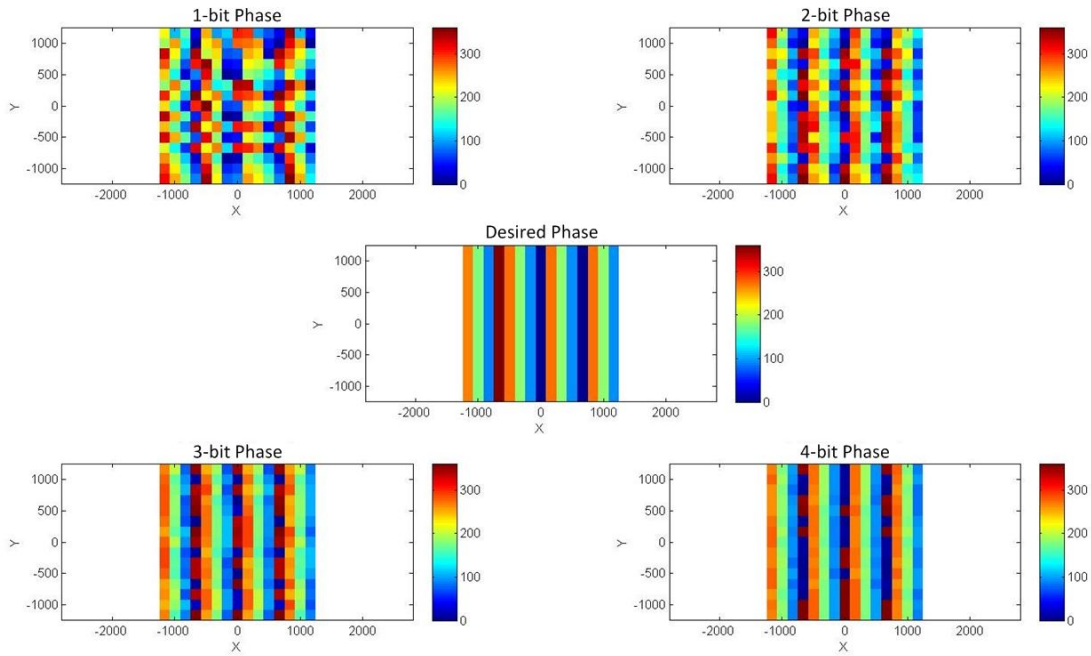
Fig. 13. Phase distribution across an aperture with n-bit phase resolution

Fig. 14 shows the impact of increased resolution on the gain patterns of the RA. The contour plots map far-field angles in the +z hemisphere to a horizontal and vertical axis representing azimuth and elevation components, respectively. Color represents radiation intensity in dB.
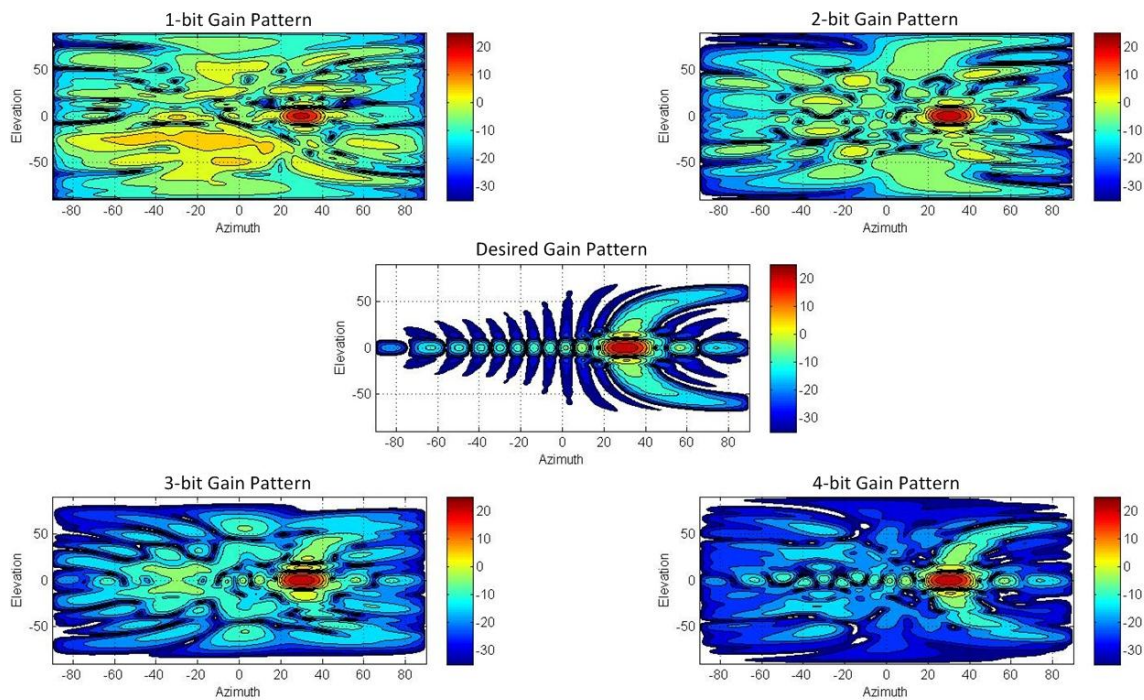
Fig. 14. Gain patterns resulting from the apertures of Fig. 13

The bright red spot in Fig. 14 (top left) at the 30° azimuth angle illustrates that even the simple 1-bit phase shifters can produce a beam in the desired direction, but the realized gain is 3 dB less than with ideal phase shifters. The large areas of yellow and orange in the same graph highlight another performance issue with low phase resolution: side

lobes. Low phase resolution inherently produces undesired levels of peripheral radiation. With increased phase shifter resolution the gain of the main lobe increases and the SLL reduces. However, each additional bit provides diminishing returns in improvement. In a general context 3-bit phase resolution provides adequate performance for most applications.

B. Material Properties

The Maxwell Garnett mixing rules in [20] help predict the aggregate electrical properties (ε_{rd}) of dispersions given the properties of the fluid medium (ε_{r1}), the particle (ε_{r2}), the volume fraction ϑ, and the particle's geometry. Fig. 15 illustrates the impact of particle aspect ratio on $\varepsilon_{rd}(\vartheta)$ for spherical (colloids), disc (flakes), and needle (whiskers) - three canonical particle geometries. This demonstrates how particle morphology can be used to achieve greater changes in the dispersion at lower volume fractions.

Fig. 15. The Maxwell-Garnett mixing rule for various particle shapes (left) and the BSTO nanoparticles proposed in this work (right)

Fig. 15 suggests that material systems using higher aspect ratio particles provide greater permittivity shifts at lower volume fractions compared with the spherical particles. Research is underway in other disciplines to produce these particles at scale [21], but at present spherical particles remain more available in bulk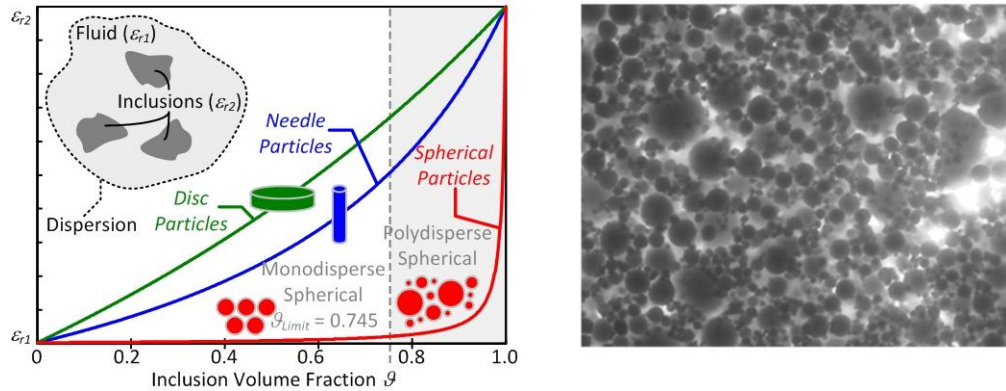 and thus the focus of this work. Equation (13) provides the mixing rule for $\varepsilon_{rd}(\vartheta)$ of dispersions using these particles. Note that ε_{r1} and ε_{r2} may be complex numbers to represent losses from dielectric dampening. The aggregate losses can be characterized with a loss tangent $\tan \delta_d$.

$$\varepsilon_{rd} = \varepsilon_{r1} + 3\varepsilon_{r1}\vartheta \frac{\varepsilon_{r2} - \varepsilon_{r1}}{\varepsilon_{r2} + 2\varepsilon_{r1} - \vartheta\left(\varepsilon_{r2} - \varepsilon_{r1}\right)} = \varepsilon'_{rd} + j\varepsilon''_{rd}$$

$$\tan \delta_d = \frac{\varepsilon''_{rd}}{\varepsilon'_{rd}} \qquad (13)$$

$$\varepsilon_{r1} = \varepsilon'_{r1} + j\varepsilon''_{r1} = \varepsilon'_{r1}\left(1 + j\tan \delta_1\right)$$

$$\varepsilon_{r2} = \varepsilon'_{r2} + j\varepsilon''_{r2} = \varepsilon'_{r2}\left(1 + j\tan \delta_2\right)$$

Fig. 16 depicts both ε'_{rd} and $\tan \delta_d$ as $\tan \delta_1$ and $\tan \delta_2$ are varied. A total of six curves represent fixing one loss tangent at a low value, drastically raising the other value, and then reversing procedure. The values $\varepsilon'_{r1} = 2.1$ and $\varepsilon'_{r2} = 500$ represent estimates of the materials used in early prototypes in this work. The curve representing ε'_{rd} in Fig. 16 (left) remains identical for all combinations of fluid and particle loss tangents. Only ε'_{r1} and ε'_{r2} have an impact here.
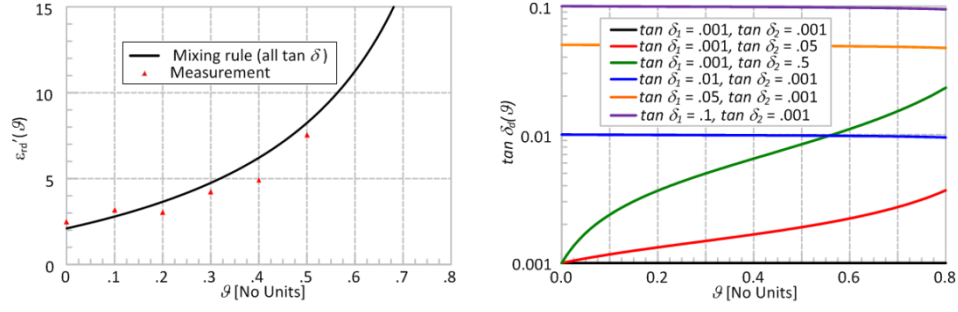
Fig. 16. The impact of material loss tangents on the aggregate permittivity (left) and loss

tangent (right)

The logarithmic scale of Fig. 16 (right) aids in viewing the dependence of tan δ_d on tan δ_1. Even extremely large values of tan δ_2 do little to shift the aggregate loss tangent an order of magnitude away from tan δ_1, especially for volume fraction $\vartheta < 50\%$. This highlights the importance of low-loss fluids in operating reconfigurable RF systems, including antennas.

C. *Coaxial Devices*

This work uses the coaxial transmission line as a platform for loading a reflectarray element. The electrical length and characteristic impedance Z_0 of the coaxial lines in Fig. 17 depend on the electrical properties of the fluid flowing through them [22]. Equation (14) links these electrical characteristics to the dispersion volume fraction, ϑ. This work takes advantage of this link to both functionalize (Fig. 17, left) and measure (Fig. 17, right) shifts in material composition.
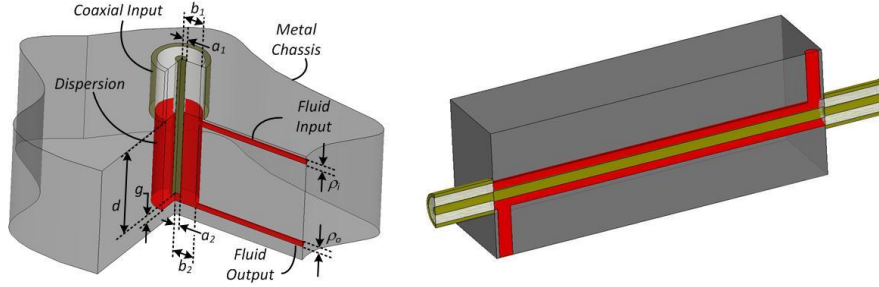
Fig. 17. A 1-port coaxial stub (left) and a 2-port coaxial measurement cell (right)

$$Z_0(\vartheta) = \frac{\eta_0}{2\pi\sqrt{\varepsilon'_{rd}(\vartheta)}} \ln\left(\frac{b}{a}\right)$$

$$\beta(\vartheta) = \frac{2\pi f}{c}\sqrt{\varepsilon'_{rd}(\vartheta)}$$

(14)

The spherical shape of the particles in this work make $\varepsilon'_{rd}(\vartheta)$ a slowly varying function (Fig. 15), so the dimensions of the coaxial line need to extend its impact on Z_0. The inner radius a_2 of the coax is fixed based on available conductive rods, but the outer radius b_2 may be adjusted to maximize the electrical impact of permittivity on Z_0. From (15) increasing b_2 raises potential range of Z_0. Fig 18 depicts the range in characteristic impedance using the material properties from Fig. 18 with $\vartheta_{low} = 0.1$ and $\vartheta_{high} = 0.5$. The radii ratios highlighted refer to various fabricated components described later in this work.

$$Z_{0,range} = \left|Z_{0,high} - Z_{0,low}\right| = \left|\frac{\eta_0}{2\pi}\ln\left(\frac{b}{a}\right)\left(\frac{1}{\sqrt{\varepsilon'_{rd}(\vartheta_{high})}} - \frac{1}{\sqrt{\varepsilon'_{rd}(\vartheta_{low})}}\right)\right|$$

(15)
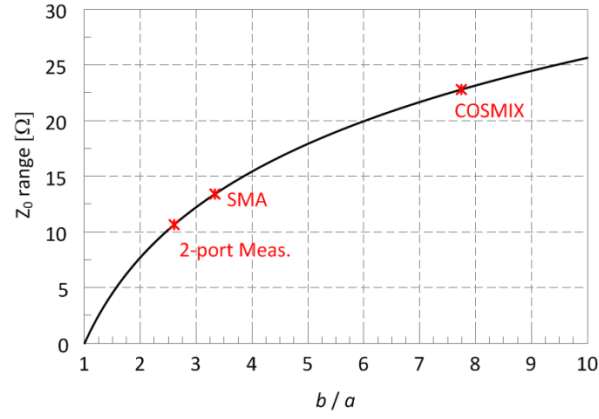
Fig. 18. The characteristic impedance Z_0 as a function of radii ratio

Another way to examine this impact is analyze the derivative of Z_0 w.r.t. the volume fraction ϑ (Fig. 19). This derivative is proportional to the natural log of the radii ratio. Hence increasing this ratio can heighten the response of Z_0 to changes in material properties.

$$\frac{dZ_0}{d\vartheta} = \frac{dZ_0}{d\varepsilon_{rd}}\frac{d\varepsilon_{rd}}{d\vartheta} = \left(-\frac{\eta_0 \ln\left(\dfrac{b_2}{a_2}\right)}{4\pi\left(\varepsilon_{rd}(\vartheta)\right)^{3/2}} \right)\left(\frac{3\varepsilon_{r1}\left(\varepsilon_{r2} - \varepsilon_{r1}\right)\left(2\varepsilon_{r1} + \varepsilon_{r2}\right)}{2\varepsilon_{r1} + \varepsilon_{r2} - \vartheta\left(\varepsilon_{r2} - \varepsilon_{r1}\right)} \right) \tag{16}$$
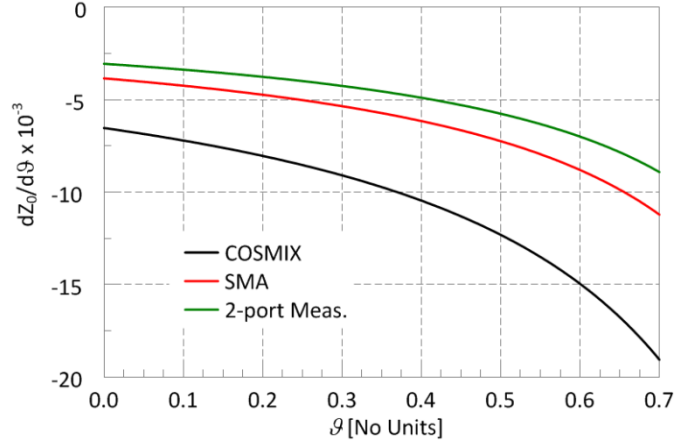
Fig. 19. The derivative of Z_0 for different radii ratios

For proper operation of the coaxial line, all modes except the dominant TEM-mode should be in cutoff. Furthermore, inlets and outlets need to be small enough to keep circular waveguide modes in cutoff, making the holes electrically invisible. Fig. 20 shows a plot of all these cutoff frequencies as the volume fraction ϑ (and the aggregate dielectric constant) increases. Even for extremely high dielectric constants the 3 GHz design frequency remains below the cutoff frequencies of spurious modes.
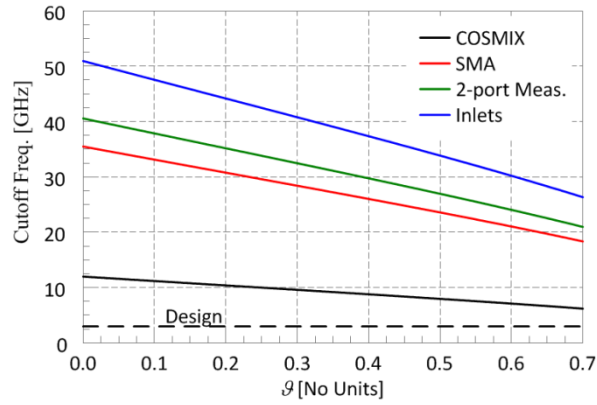
Fig. 20. Cutoff frequencies of spurious modes in various components

i. COSMIX

The Coaxial Stub Microfluidic Impedance Transformer (COSMIX) of Fig. 17 (left) operates on the parameters of the coaxial line but features a capacitive gap termination characterized in [23] by Eq. (17). Fig. 21 depicts the T-Line model of the COSMIX and highlights the dependence upon material composition within. Fig. 22 plots the input impedance as seen by a coaxial device connected to the COSMIX using the theoretical model and simulated model in HFSS [24]. The COSMIX in this model features SMA dimensions ($a = 0.615$ mm, $b = 2.05$ mm), a gap of $g = 0.5$ mm, and various lengths of d. The COSMIX is filled with a dispersion modeled with $\varepsilon_{r1} = 3$, $\varepsilon_{r2} = 500$ and $\tan \delta_1 = \tan \delta_2 = 10^{-3}$.
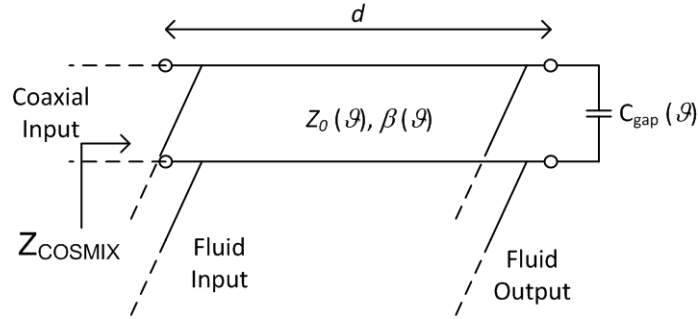
Fig. 21. T-Line representation of COSMIX

$$C_{gap} = \frac{\varepsilon \pi a^2}{g} + 4 a \varepsilon \ln \frac{b-a}{g} \tag{17}$$

The results shown correspond to the frequency of interest, 3 GHz. The imaginary part of the input impedance - the reactance - varies from $-\infty$ to $+\infty$ with a starting point

depending upon the length of the COSMIX as the volume fraction is adjusted. The expression in (17) does not perfectly capture the behavior of the capacitive gap and results in a slight offset between the theoretical and simulated results. However, the trends are in excellent agreement. This structure represents an ideal loading mechanism capable of the full spectrum of reflect phase at its interface. The resistance remains close to zero except when the COSMIX cycles through an open circuit impedance. Furthermore, inlets with $\rho = 1.984$ mm have virtually no effect on the simulated results.
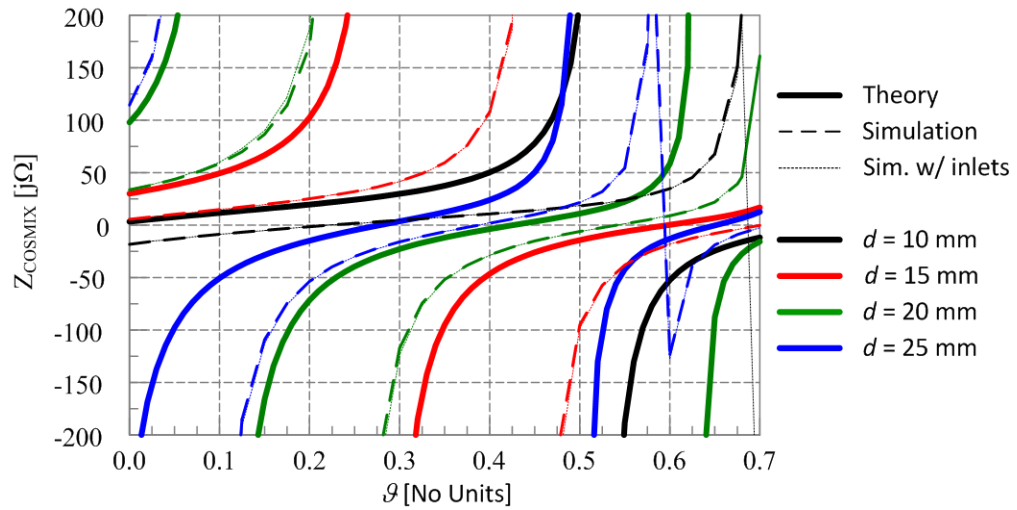
Fig. 22. Theoretical and simulated input impedance of the COSMIX

It should be noted that this impedance reconfiguration relies heavily on the capacitive gap. Fig. 23 shows the simulated impedance results if the gap is shorted out (i.e. $g = 0$). The agreement between theory and simulation in these results confirms the capacitive gap as the source of error in the results of Fig. 22. A shorted COSMIX may still successfully operate as a reconfigurable loading mechanism, but the impedance provided

will substantially shift when compared to the COSMIX with a gap. Consider the simulated curves for a d = 10 mm COSMIX (black traces of Fig. 22 and Fig. 23). Simulations indicate the COSMIX with the gap can provide a -j30 Ω to +j30 Ω impedance range with a volume fraction ϑ < 60%. Shorting the gap limits the ability of the COSMIX to provide this impedance range with the same constraint on ϑ. The shorted COSMIX must compensate with a longer length which is undesirable.
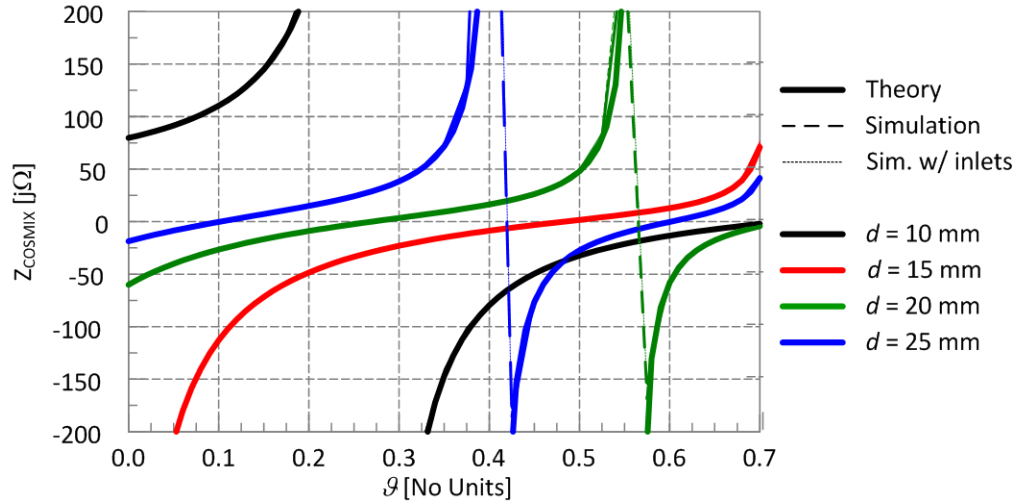
Fig. 23. Theoretical and simulated input impedance of shorted COSMIX

ii. 2-Port Measurement Cell

The measurement cell of Fig. 17 (right) features a hollow coax line in an aluminum fixture with SMA adapters mounted on the outside to allow for 2-port S-parameter measurements. Many transmission line techniques can process S-parameter measurements and calculate material properties [25]. MATLAB scripts which utilize

these techniques and account for a discontinuity in coax inner radii [23] are under development.

D. Microstrip Patch RA element

Fig. 24 shows a CAD model of the proposed RA element using the COSMIX reactive loading mechanism. The RA element is a microstrip patch of a resonant length L and width W atop a substrate of height h and permittivity ε_{rs}. The COSMIX is centered about the patch width at $W/2$ and placed a distance s from one of the radiating edges. The resulting topology is similar to a coaxial probe-fed patch in appearance only.
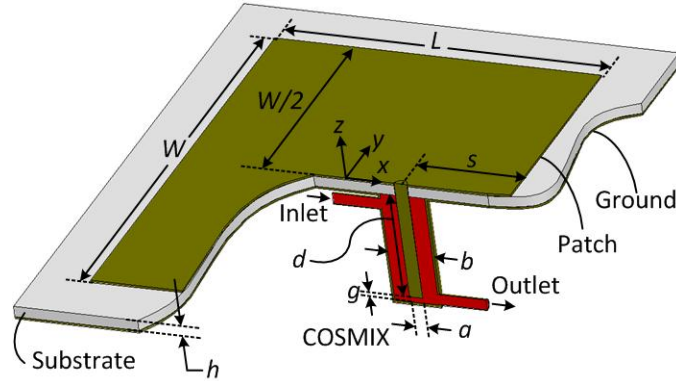
Fig. 24. Physical parameters of a microstrip patch RA element and COSMIX

Fig. 25 combines the T-line model of the COSMIX (in red) with the well-known model of the microstrip patch (in black) to predict the reflect-phase behavior of the element. The patch dimensions and relevant equivalent parameters can be synthesized from design equations easily accessible in the open literature [18]. The model here removes

the slot susceptance in lieu of the equivalent length extension ΔL. The model for the patch also includes an equivalent inductance in series to represent the coaxial probe.
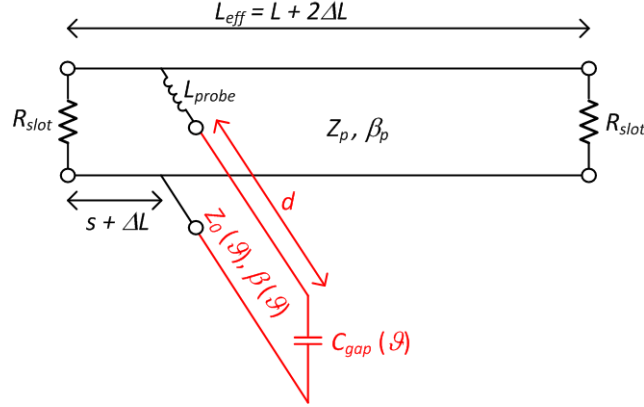
Fig. 25. T-line model of RA element

Two different methods for analyzing the phase of the RA element reflection have demonstrated moderate success. The work by Venneri in [26] examines the interface between the patch and the loading mechanism. The terminals AA´ represent the equivalent interface of the design of this work. Fig. 26 separates the COSMIX from the patch to look at two different impedances, Z_{patch} and Z_{COSMIX}. The Thevenin equivalent circuit of Fig. 26 provides the reflection coefficient, $\Gamma_{V,}$ of (18).
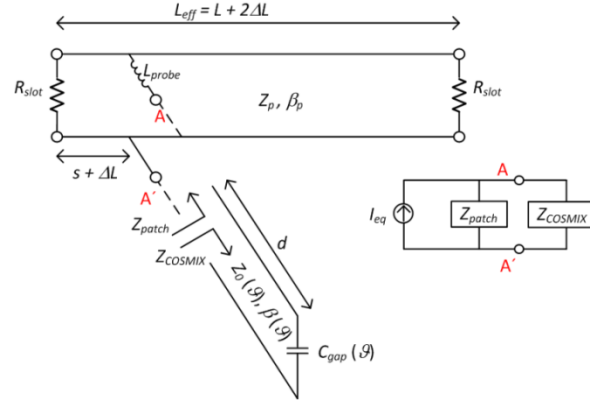
Fig. 26. Thevenin equivalent RA element using Venneri's method

$$\Gamma_V = \frac{Z_{COSMIX} - Z_{patch}}{Z_{COSMIX} + Z_{patch}} \tag{18}$$

Hum examines the interface between one of the radiating slots and the rest of the element in [27]. This approach more intuitively represents a wave interacting with the RA element. The Thevenin equivalent in Fig. 27 shows how this method applies to the RA element of this work to provide the reflection coefficient Γ_H.
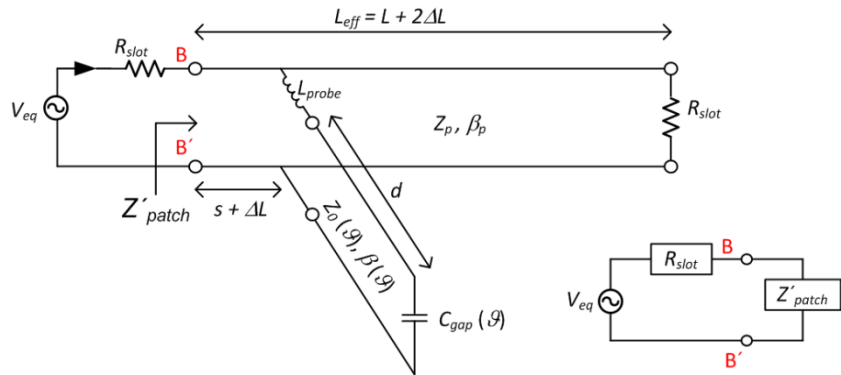
Fig. 27. Thevenin equivalent of RA element using Hum's method

$$\Gamma_H = \frac{Z'_{patch} - R_{slot}}{Z'_{patch} + R_{slot}} \tag{19}$$

Fig. 28 compares the predicted phase shift of the two models with that of a rectangular waveguide (RWG) simulation. The RWG simulation represents the benchmark for the models since its accurately emulates a plane wave incident upon a reflectarray unit cell [27]. The patch element ($L = 30.8$ mm, $W = 39.4$ mm) sits atop a Duroid 5870 substrate ($h = 125$ mil, $\varepsilon_r = 2.33$, $\tan \delta = 1.2$ x 10^{-3}). An equivalent impedance replaces the full model of the COSMIX to mitigate discrepancies in the model of the capacitive gap. A parametric study moves the COSMIX from $s = 2$ mm from the radiating edge toward the center of the patch in 4 mm steps. All the phase curves have been manually centered about 0° for easier comparison. Changes in the input impedance of the COSMIX shift the phase of the reflection coefficient in all models. In all cases the phase curves slope downward and in increased intensity as the COSMIX moves closer toward the center of the patch. Neither model accurately captures the expected phase behavior though. Given the successful modeling demonstrated in [26, 27], the method of applying the circuit models of previous works to this work may be the likely source of error.
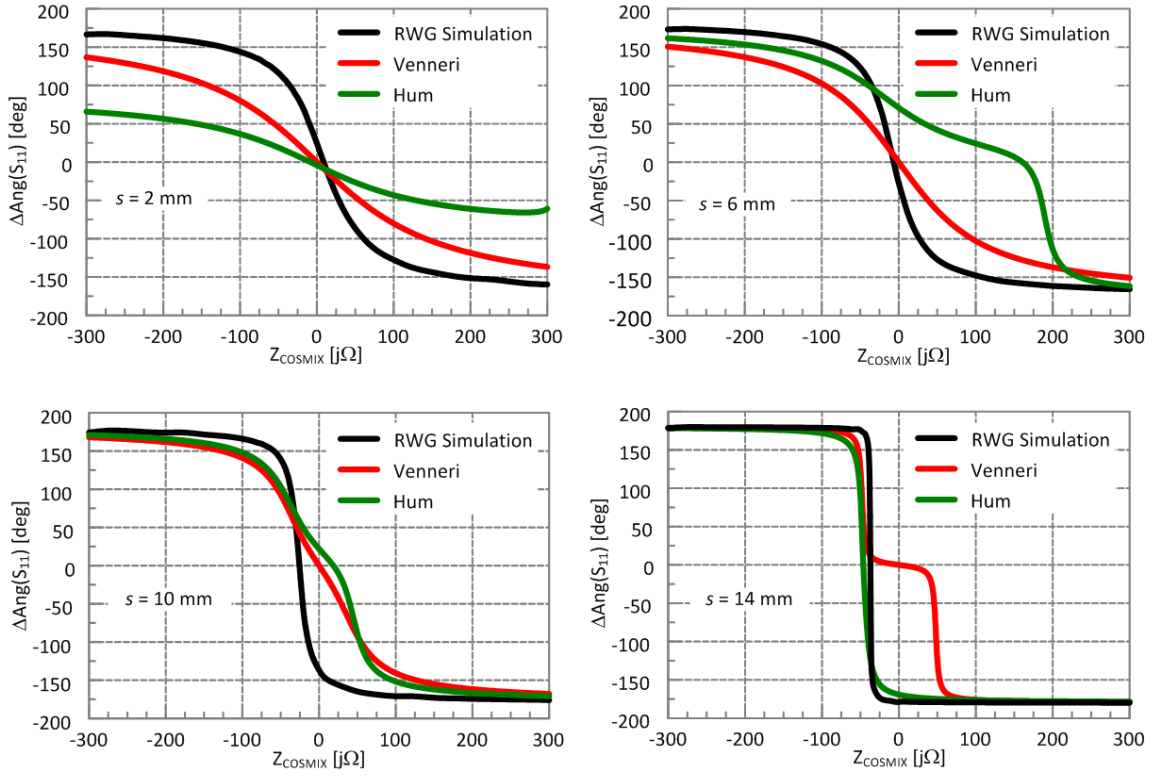
Fig. 28. Theoretical and simulated phase response to an impedance loaded RA element

E. Contributions

The formulas and plotting routines developed here provide performance metrics of a RA. They also serve as valuable tools for future RA schemes. Examining the role physical dimensions and material properties play in the electrical behavior of coaxial topologies helps to extend the impact material composition has on the input impedance of these devices. The T-line models demonstrated here serve as valuable tools to understanding the interaction between the RA element and the COSMIX loading mechanism.

CHAPTER IV

FIRST ITERATION

A. Simulation

Fig. 29 shows a CAD model of the first iteration of the RA element. The patch is cut

from copper sheet and rests atop a Rohacell foam substrate (h = 3.75 mm, ε_r ~ 1, and tan

δ ~ 0). The dimensions W = 50 mm and L = 44.5 mm come from design equations [18]

for operation at 3 GHz. A simple hole in an aluminum GND plane and attached metallic

block forms the COSMIX. The parameters of the COSMIX were chosen similar to [28]

with a = 2.05 mm, b = 0.615 mm, and g = 0.5 mm. A 1 mm thick gear-shaped Teflon

spacer was placed around the probe to keep it centered within the COSMIX. The notches

cut into the spacer allow the dispersion to flow through the spacer during material

injection.
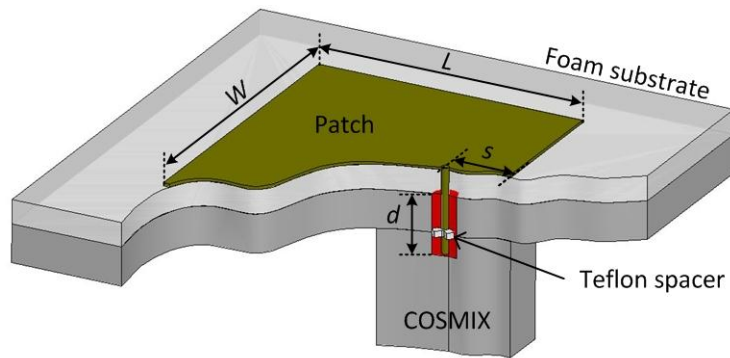
Fig. 29. First iteration of RA design

For measurement, the RA element rests at the bottom of a rectangular waveguide (see Fig. 30) with reflecting walls that emulate an array environment with unit cell dimensions A_2 and B_2. The probe launch is a WR-284 circular flange with $(A_1, B_1) =$ (72.14 mm, 34.04 mm). The expanded dimensions $A_2 = B_2 = 80$ mm were chosen to minimize interactions between the patch and the waveguide walls. These dimensions create a 38.68° angle of incidence and an accurate approximation of trends in performance at angles closer to broadside. This does not mimic the intended array environment, but it does provide an opportunity to make observations on the isolated RA element.
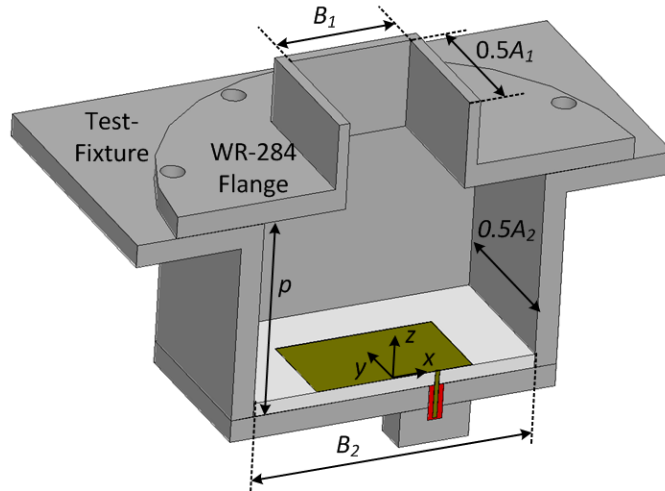
Fig. 30. First iteration of RA element in waveguide test fixture
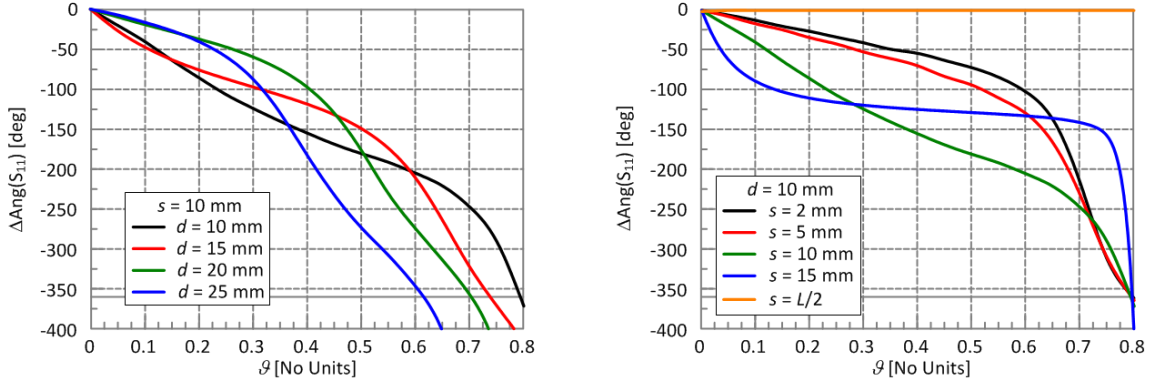
Fig. 31. Simulated phase of the waveguide by varying *d* (left) and varying *s* (right)

Prior to the development of the circuit model in the previous chapter, a series of parametric studies examined the impact of several design parameters on the performance of the RA element. Fig. 31 shows an example of these results. The materials used in the simulation were a silicone fluid (ε_{r1}, tan δ_1) ~ (2.68, 10^{-3}) loaded with spherical nanoparticles (ε_{r2}, tan δ_2) ~ (500, 10^{-3}). The simulated results of Fig. 31 (left) are for a COSMIX placed *s* = 10 mm from the radiating edge with a variable length of *d*. The physical operation of the RA element may benefit from reducing the size of the COSMIX, and the results indicate a length longer than *d* =10 mm does not necessarily provide a better phase response, especially at lower volume fractions. The position of the COSMIX is also a very important parameter. It affects how the impedance shift at the reference plane of the COSMIX translates into the phase shift at the reference plane of the patch. Fig. 31 (right) shows the simulated results from sweeping *s* over a range of values from 2 mm to *L*/2. The location *s* = 10 mm provides a nearly phase linear response which will aid in early experiments. The location *s* = *L*/2 represents a quasi-

zero field point in the TM_{10} mode of the patch (see Fig. 4). Placing the COSMIX here is equivalent to placing it in shunt with a virtual short. The zero phase change observed here verifies the resonant mode of the patch.
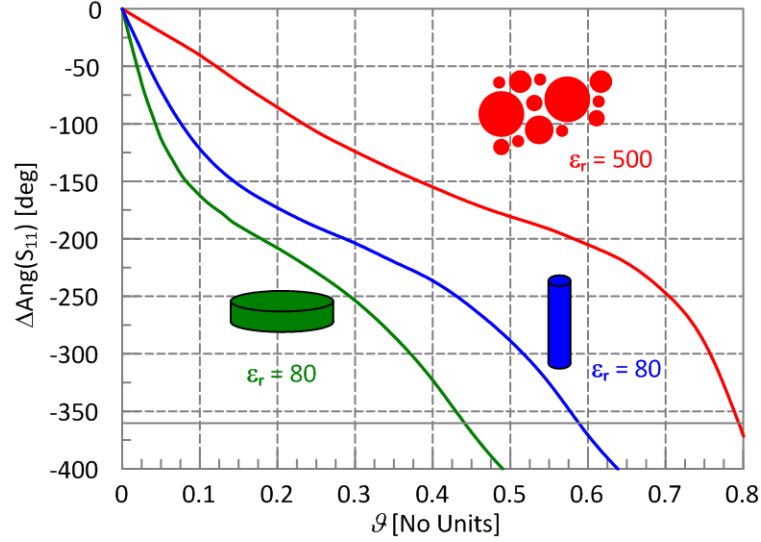
Fig. 32. Impact of particle aspect ratio and dielectric strength in the dispersion on the phase-change of the RA element

Simulations also investigated the impact of material composition on the reflection behavior. Fig 32 depicts the phase performance for designs with various mixing rules [20] representing canonical particle geometries with a height-to-diameter aspect ratio τ. This includes spheres ($\tau = 1$) with $\varepsilon_{r2} = 500$, rods ($\tau = 0.1$) with $\varepsilon_{r2} = 80$, and disks ($\tau = 10$) with $\varepsilon_{r2} = 80$. The results illustrate a strategy (even when compensating for much lower dielectric strength ε_{r2}) to reduce the necessary volume fraction for the desired 360° shift from $\vartheta = 79\%$ (spheres) to 59% (rods) to 44% (disks). Material losses were

included as tan $\delta_2 = 0.001$ but resulted in negligible attenuation for this particular design. Fig. 33 shows the impact of dielectric losses on the reflection performance. Simulations used the mixing rule for spherical particles and varied the loss tangent of both the fluid medium and the particle. The results intuitively track with the predictions from Fig. 16. The loss tangents in all cases have no impact on the phase shift, and only the loss tangent of the fluid significantly influences the attenuation in the reflected signal.
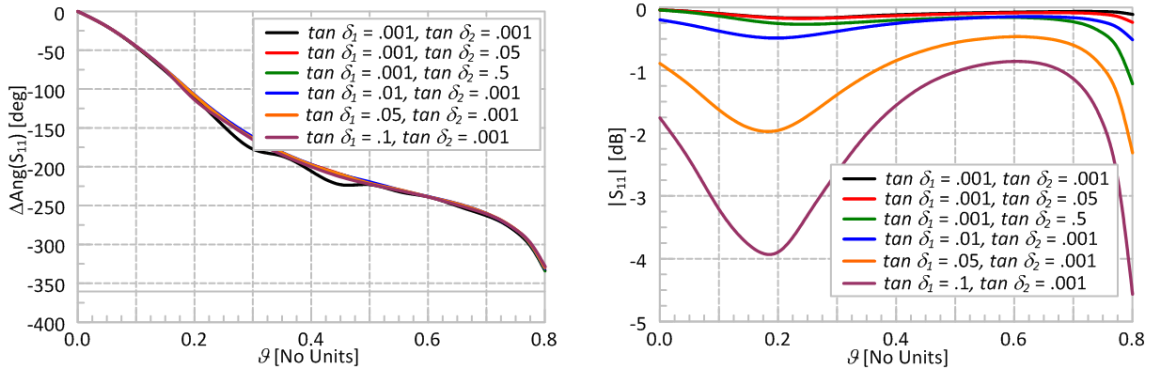
Fig. 33. Impact of material loss tangents on the phase shift (left) and return loss (right)

B. Experiment

Fig. 34 shows the test fixture and RA element with $s = d = 10$ mm fabricated to experimentally observe the system. The fixture and flange were machined from 6.35 mm (.25 in) thick aluminum plates and the patch was cut from a 1.0 mm thick copper sheet. The Teflon spacer was cut from a section of dielectric sleeve in an SMA probe, giving it the appropriate radii for the COSMIX. Polydispersed colloidal BSTO [29] ($\varepsilon_{r2} \sim 100$ and *tan* $\delta_2 \sim 0.5$, diameters < 800 μm) was weighed out and mixed into silicone oil [30] to

produce volume fractions from 0% to 50% in 10% increments. Repeated sonication to reduce particle aggregation and vortexing for vigorous mixing resulted in homogeneous dispersions. Finally, the dispersion was stirred by hand until qualitatively considered a 'good' dispersion (e.g., it flowed well and did not show any aggregation).
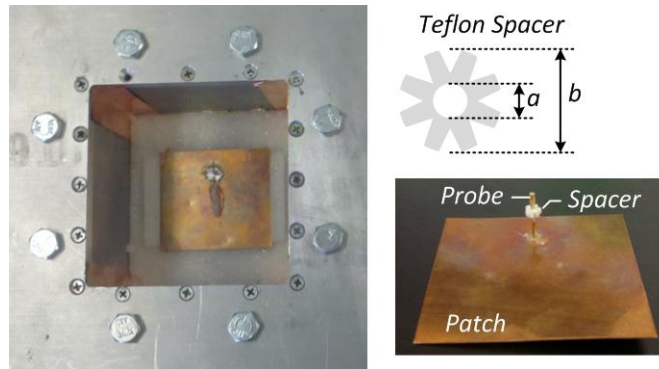
Fig. 34. Fabricated proof-of-concept for the RA element

A dielectric probe [31] measured the electrical properties of the dispersions prior to their injection into the COSMIX. The test fixture was partially disassembled to allow manual injection of the dispersion (Fig 35). After reassembly a network analyzer [32] measured the magnitude and phase of signals reflected from the patch. Between measurements the fixture was disassembled for thorough cleaning.
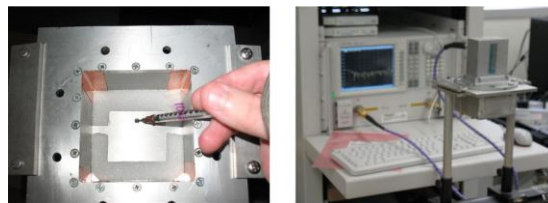
Fig. 35. Replacing material in the COSMIX (left) and measurement of reflection (right)

C. Results

These material measurements of Fig. 14 show excellent agreement with the Maxwell-Garnett mixing rule's predictions. Fig. 36 shows the measured reflect phase at the design frequency of 3 GHz along with the simulated results (with and without the Teflon spacer). The fabricated element achieved up to 200° of phase shift while experiencing a return loss of less than 1.2 dB. Measurements of the empty waveguide indicated a 0.4 dB baseline loss which, in part, contributes to the measured return loss values exceeding simulated values. Other discrepancies between the simulated and measured results stem from inaccuracies in material data and the lack of a waveguide calibration kit.
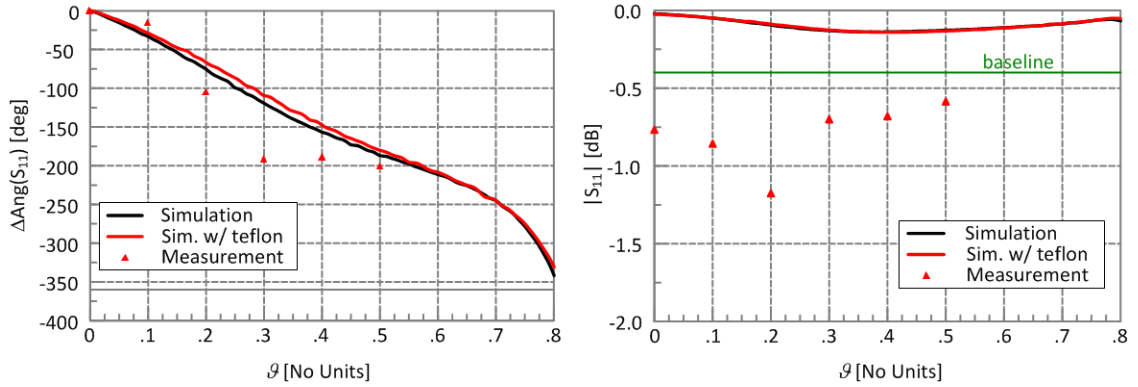
Fig. 36. First measurement of COSMIX and RA element in a waveguide

A series of five experiments were performed later with a newly acquired waveguide calibration kit. Fig. 37 compares these results with simulations involving materials with greater loss tangents. The error-bars illustrate the deviation among the measurements and indicate the widest error in phase occurred at a volume fraction of $\vartheta = 20\%$. Trends

in the simulated and measured results agree very well. The traces representing the simulated phase shift fit reasonably within the deviations of the measurement and the measured return loss slopes in a manner similar to the simulated values.
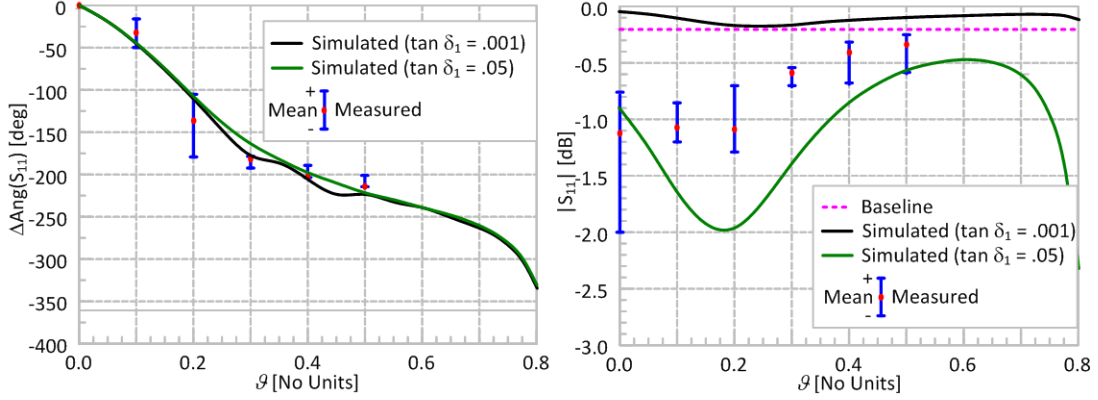
Fig. 37. The measured reflect-phase (left) and return loss (right) of the first RA prototype

D. Contributions

Prior to the development of a circuit model, the simulations and parametric studies used here provide initial investigations into whether or not the notion of using material perturbation in the RA has any merit. The simulated phase shift curves establish this merit and provide the justification for experiments. These experiments and their results proved the possibility of RA phase manipulation through altering dispersion composition in the COSMIX. These experiments proved the concept and justified continuing efforts to better apply the concept.

CHAPTER V

SECOND ITERATION

A. Modifications

The proof-of-concept experiment provided promising results but highlighted several

considerations for fabrication and operation of future designs. Based on these

considerations, the waveguide of Fig. 38 now represents a smaller unit cell (50 mm x 80

mm or .5 λ_0 x .8 λ_0) for a reduced discontinuity [23] with the WR-284 flange. A

mechanically milled patch on a substrate of Duroid 5870 (h = 125 mil, ε_r = 2.33, tan δ =

1.2 x 10^{-3}) replaces the Rohacell foam and the hand-cut copper sheet of the first

experiment. The substrate introduces more loss, but this fabrication method provides

greater precision in the dimensions of the patch, the probe placement, and the orientation

of the patch in the waveguide. The (thick) substrate replaces the Teflon spacer in

securing the axial orientation of the probe. Furthermore, the dielectric constant of

substrate reduces the physical size of the patch (L = 30.4 mm, W = 39.8 mm) allowing it

to fit in the smaller unit cell. Nylon screws tighten the substrate against the ground plane

to eliminate leakage from the COSMIX but do not interfere with the performance of the

RA element. The fluidic channels in the COSMIX replace the static material injection

method of the first experiment and enables dynamic measurements with a closed-loop

fluidic system. The channel diameter of ρ = 1.984 mm (5/64 in.) allows for the insertion

of blunt syringe tips. A milling bit replaces the previously used drilling bit in the

fabrication to ensure a flat bottom when boring out the COSMIX. The outer radius of the

COSMIX increases from 2.05 mm to $b_2 = 4.7265$ mm (3/16 in.) representing the smallest milling bit available in the machine shop in the engineering building. The inner radius remains $a_2 = 0.615$ mm (.05 in) representing the available conductive rods in the laboratory. The gap remains $g = 0.5$ mm representing reliable fabrication tolerances.
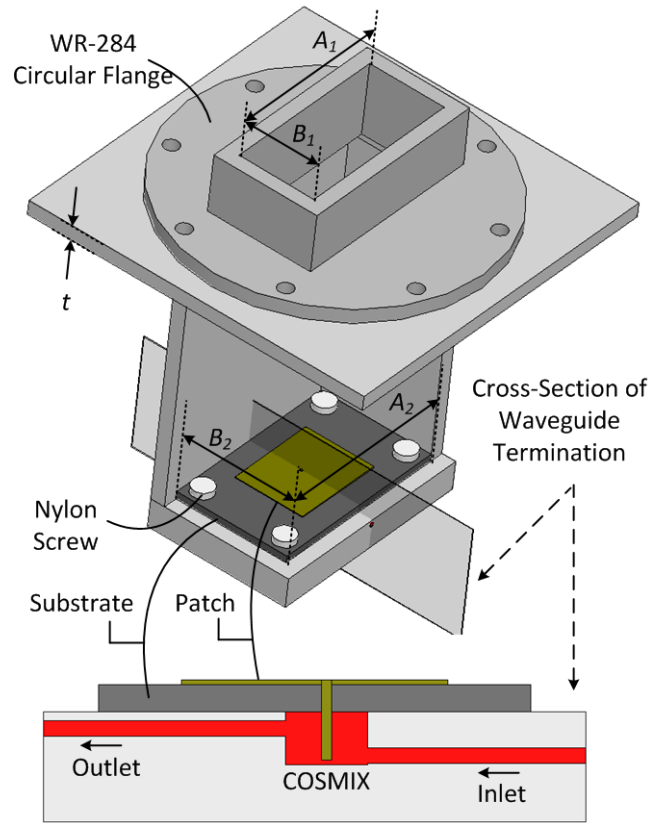
Fig. 38. Second iteration of RA element and test fixture

B. Simulation

With most other dimensions set by fabrication considerations and design equations, the remaining parameters to adjust are the COSMIX length d and position s. The loading

mechanism is isolated within the GND structure, so these parameters can be piecewise studied (an advantage compared to other topologies) for increasing phase response for volume fractions below 25%. This process starts by replacing the COSMIX in the simulated model with an equivalent impedance via a lumped port shown in Fig. 39. The impedance was swept from -j300 Ω to +j300 Ω (representing the potential input reactance from the COSMIX) as the COSMIX position was moved along the length of the patch. The phase curves of Fig. 34 (right) demonstrate that as the probe is moved closer and closer to the middle of the patch, the reflected phase becomes more sensitive to impedance changes at the reference plane of the COSMIX. Placing the probe in the middle of the patch (*L*/2) results in no phase change just as in the first prototype.
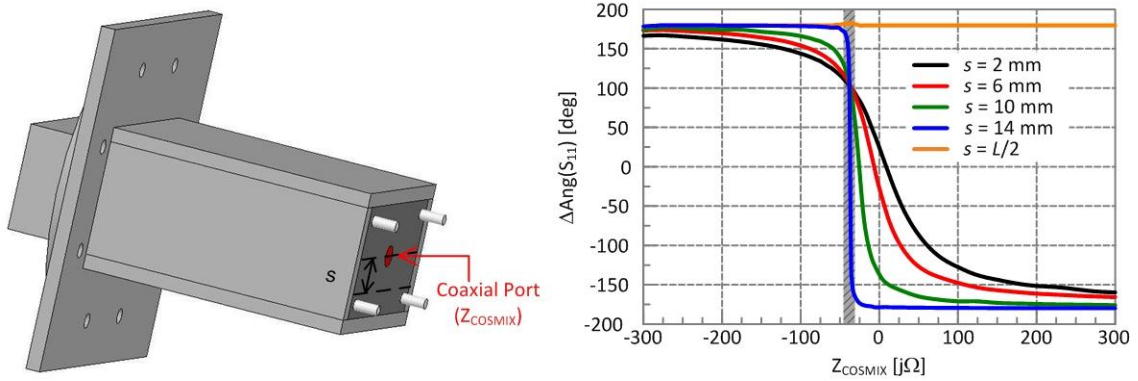
Fig. 39. COSMIX replaced with equivalent impedance (left) and resulting phase shift (right)

Selecting *s* = 14 mm provides greater potential phase shift. The impedance of roughly -j45 Ω to -j30 Ω (shown in gray shadow) produces the majority of the phase change, and

represents the design goal for the COSMIX. A separate simulation of the COSMIX tunes the remaining dimension, d, to provide a suitable impedance. The dispersion properties in the simulation were (ε_{r1}, $\tan \delta_1$) = (3, 10^{-4}) and (ε_{r2}, $\tan \delta_2$) = (500, 0.05). The exact dielectric properties of the materials were uncertain and these value represent a conservative estimation. The simulated COSMIX results (Fig. 40, right) indicate a length of d = 6 mm provides the desired impedance (grey shadow) at lower volume fractions. Selecting a length of d = 7 mm puts risks the input impedance missing the desired range entirely should the materials in the experiment have higher dielectric constants or should the fabrication process bore the COSMIX deeper than intended.
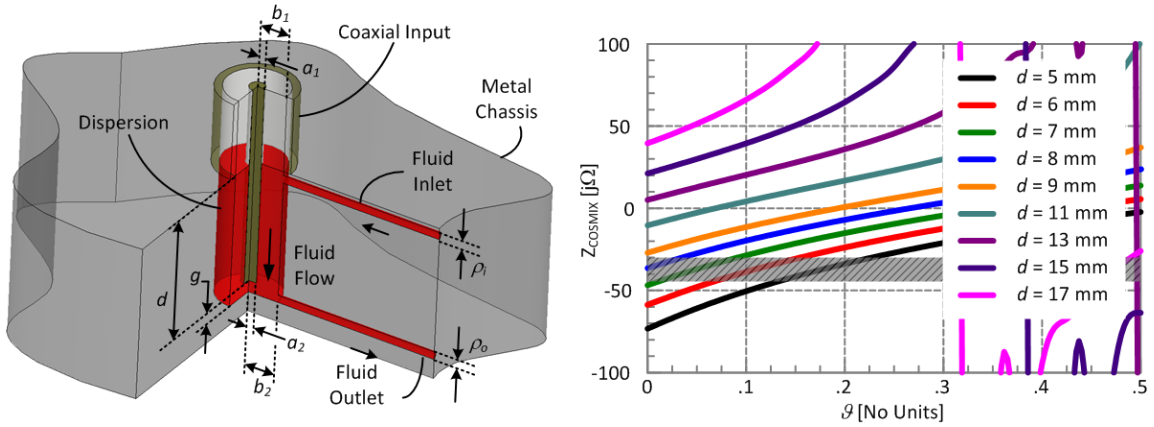
Fig. 40. COSMIX with all physical parameters (left) and the input impedance as the length is altered (right)

The optimized length and position of the COSMIX yield the simulated results of Fig. 41. More than 350° of phase change occur with a volume fraction less than 15%. Simulations of the first prototype required a volume fraction close to 80% to achieve a

similar goal. This emphasis on a steep phase response results in a natural tradeoff: greater peak loss. Compared with the first prototype this is a substantially more resonant element. Plotting the derivative of the phase illustrates the link between the phase response and the losses. Even with a relatively lossless dispersion the element has a peak loss of ~2 dB.
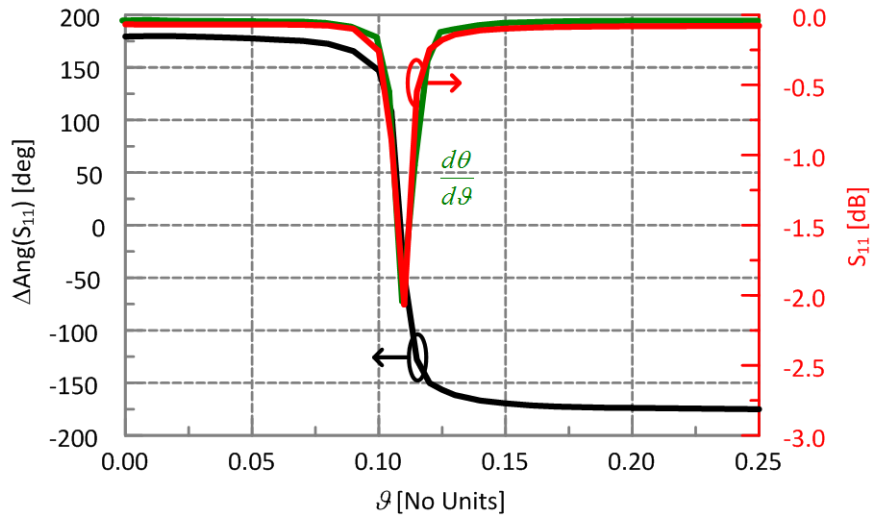
Fig. 41. Simulated phase shift and loss of the second prototype

C. Experiment

The measurement setup in Fig. 42 allows for simultaneous operation of the fluidic network, the Agilent dielectric probe, and the network analyzer for measuring the phase and loss of the RA element as the fluid is manipulated. An Agilent DC supply drives a peristaltic pump to continually circulate the dispersions between the COSMIX and a reservoir. A magnetic stirrer keeps the material in the reservoir agitated. The experiment begins with a high volume fraction of $\vartheta = 20\%$. After several minutes of circulation and

repeated phase and loss measurements to confirm operational stability, the dielectric constant of the dispersion is measured, and an injection of oil into the reservoir dilutes the dispersion by 2%. This was repeated until the volume fraction reached 8%. In the first run of the experiment no phase shift or resonances were observed. It was later discovered that the capacitive gap of the COSMIX had been shorted out ($g = 0$ mm) in fabrication. The fabrication error was corrected, and the experiment was repeated.
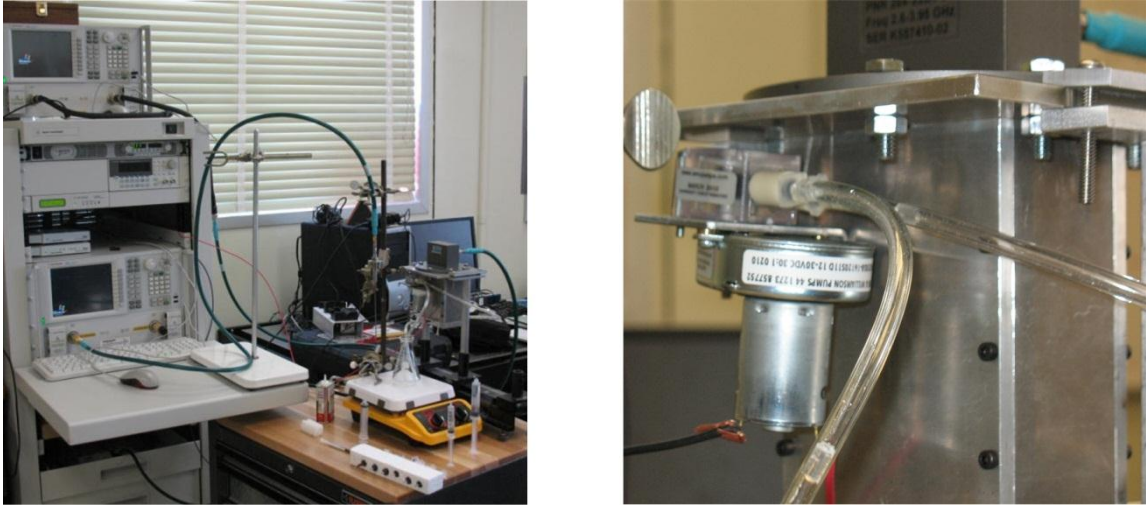
Fig. 42. Test bench for RA element (left) and custom waveguide with pump (right)

D. Results

The results of the second run are shown below in Fig. 43. The phase is normalized to the initial state with $\vartheta = 20\%$. These results indicate the RA was significantly underperforming. The losses are much greater than in the initial experiment. In each measurement three resonances in $|S_{11}|$ can be seen. One is close to 2.75 GHz. Another is close to 2.88 GHz. And yet another resonance is observed shifting to a higher frequency

with each injection of oil into the reservoir. As any of these "dips" pass through a frequency, the reflect-phase at that frequency shifts. Although phase shift consistently occurs with each injection, the operating frequency - 3 GHz - experiences little to no phase shift.
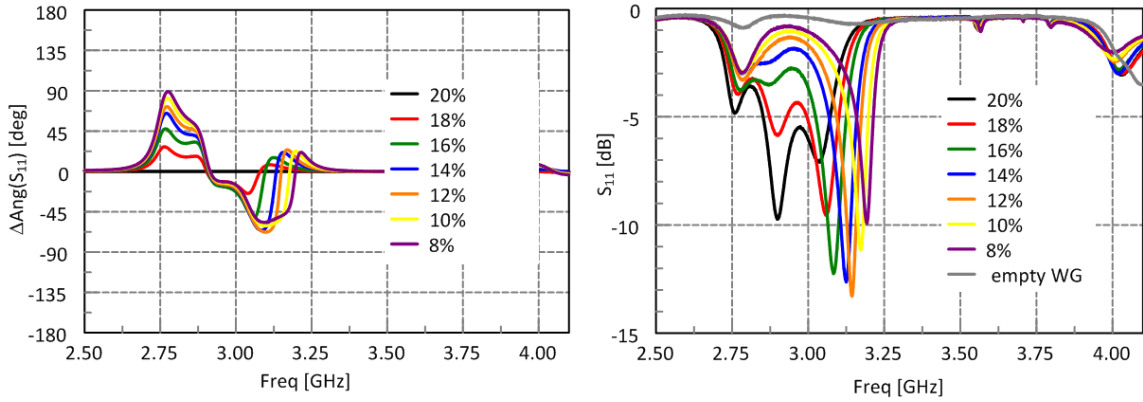
Fig. 43. Measured phase shift (left) and loss (right) of the second prototype

The materials used in this experiment came from a different batch than in the initial experiment. Studies of these materials in a SIW tunable filter [9] reveal that the actual properties of the BSTO may be closer to ε_{r2} ~100, tan δ_2 ~0.5. The particle size is likely a contributor to these less favorable properties [33]. The oil used is polydimethylsiloxane (PDMS) terminated. Work in [16] characterized its (cured) properties at RF as ε_{r1} ~2.68, tan δ_1 ~.04. The latter number represents heaviest contributor to the losses in the experiment since the properties of the fluid dominate here (Fig. 2). Fig. 44 shows the simulated results using these material properties. Similar trends in these results confirm suspicions regarding the materials used.
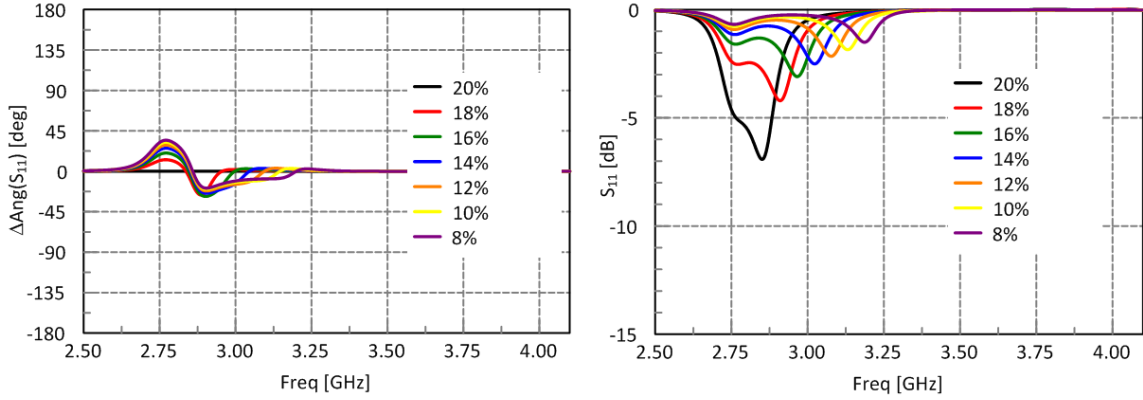
Fig. 44. Simulated phase shift (left) and loss (right) of the second prototype with

adjusted material properties

The simulated phase shift when normalized to an initial state appears worse than the measurements. In fact, this highlights a possibly critical weakness in how the experiment is run. The phase response in Fig. 41 is steep enough that a 2% volume fraction resolution may fail to observe the area of extreme shift (i.e. may miss a critical data point at $\vartheta = 0.15$). Increasing the range and resolution of the measured volume fractions mitigates this possibility by ensuring values within the steep curve are measured. Another significant factor hindering the accuracy of the measurement was the lack of a waveguide calibration kit. Fig. 45 depicts the results of repeating the measurement with the calibration kit and with many more volume fractions. The phase of the reflected signal and the dips in $|S_{11}|$ consistently shift with every injection of oil. Only two distinct dips are present which is in agreement with simulations. Fig. 46 depicts the results for the operating frequency – 3 GHz. A phase shift greater than 270° occurs and the trends suggest expanding the range of volume fractions (going past $\vartheta = 15\%$) would demonstrate even more phase change.
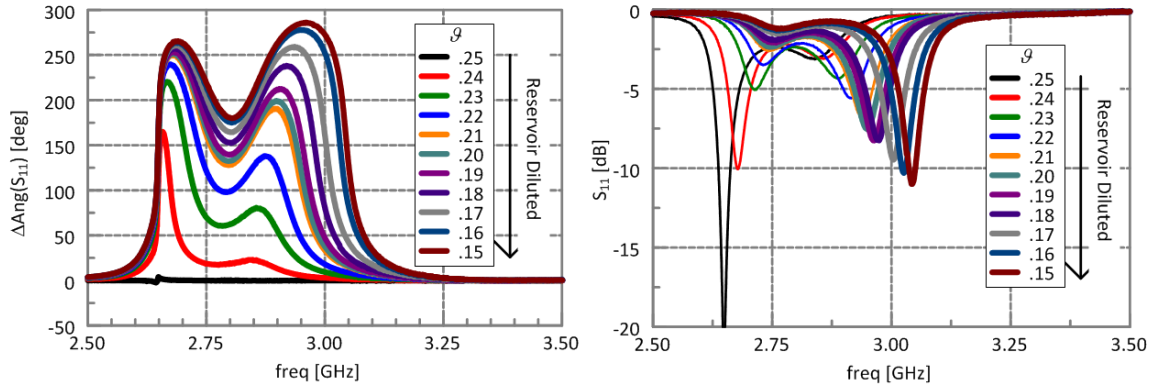
Fig. 45. Measured phase shift (left) and loss (right) of the second prototype with

waveguide calibration and more values of ϑ
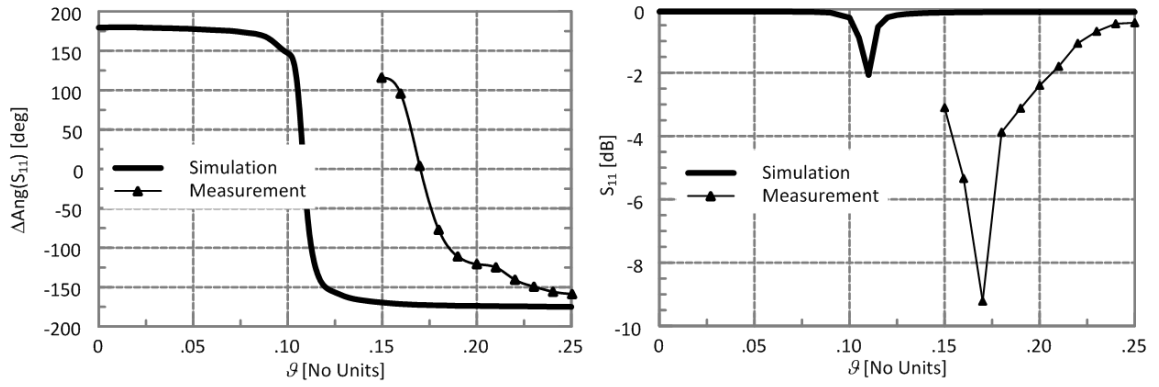
Fig. 46. Comparison between the simulated and measured results at 3 GHz for phase

(left) and return loss (right)

E. Contributions

This prototype demonstrates a significant leap forward in the RA design process by providing intuitive objectives for the dimensions and placement of the loading mechanism. No such objectives existed in the design process for the first iteration of the RA element which relied on extensive parametric studies to produce an element for fabrication. The measurement setup attempts the first ever use a circulatory system to control an RA element and refines the concept proven in the previous experiment. The results further demonstrate potential of using a circulatory system with a dynamic material to manipulate an RA element. The large values of return loss provide a more accurate picture of those materials to improve further designs.

CHAPTER VI

THIRD ITERATION

A. Modifications

The third iteration of the design is shown in Fig. 47. The fluidic network has been redesign for a layered ground plane to make fabrication easier (drilling the thin channels deep into a solid GND can easily break a drill bit). The lateral lines of the previous prototype are replaced with vertical feeds to make room for adjacent elements in an array. A 2-port coaxial fixture for material measurement may attach in series with these feeds, replacing the Agilent dielectric probe kit used in previous measurements for true *in situ* material data (use of the dielectric probe required turning off the pump and moving the reservoir). The feeds run into rectangular, trenched channels with a width $w_{\text{ch}} = 2\rho$ and a height of h_{ch}.
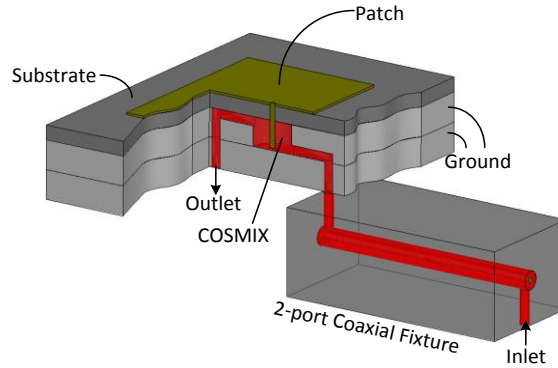
Fig. 47. The third prototype RA element with attached measurement fixture

The layered GND plane removes the need for a milling bit to achieve a flat bottom, so the COSMIX diameter depends on available drilling bits instead. The greater variety of drill bits allows for a potential reduction in the outer diameter of the COSMIX. However, the new layout limits the COSMIX length d is to available metal thicknesses. Specifically d is restricted to 6.35 mm (.25 in. aluminum).

The test fixture also features modifications. The waveguide width was set identical to the WR-284 adapter ($A_1 = A_2 = 72.14$ mm) to minimize discontinuity at the junction. The waveguide height remains $B_2 = 50$ mm to physically accommodate the patch. The flange between the adapter and the waveguide provides a taper to alleviate the discontinuity.

$$B_{flange} = \frac{B_1 + B_2}{2} = 42.02mm \tag{20}$$

B. Simulations

An increase in material velocity reduces the speed and likelihood of material buildup in regions within the COSMIX. Simulations [34] of the fluidic network examined the potential benefit of reduced a COSMIX diameter to increase material velocity in the capacitive gap. Fig. 48 shows cut planes illustrating the velocity profile. In all cases, the majority of material travels in a direct path from the inlet in the COSMIX, to the outlet. Relatively very little material movement occurs in the capacitive gap, though reducing the diameter of the COSMIX (slightly) alleviates this issue. Reducing the channel height to $h_{ch} = 0.5$ mm has a similar effect.

Fig. 48. Velocity profile in the COSMIX for various COSMIX diameters

While a reduced COSMIX diameter is (slightly) beneficial to the fluidic system, its impact on the phase performance is of greater priority. The RA element again goes through a separable design process, but in a reverse order from before. Simulations consider impedance of the COSMIX first. Fig. 49 shows the COSMX simulated with a fixed length of $d = 6.35$ mm, gap of $g = 0.5$ mm, and with the outer radius adjusted. The materials in the simulation contain feature accurate estimates for material losses (actual tan δ of the materials is still uncertain). Increasing the diameter reduces the range of impedance provided. As suggested in Chapter III, the larger radii ratio benefits the

impedance reconfiguration of the COSMIX. The outer radius of the COSMIX remains at its previous dimension of $b_2 = .375$ in.
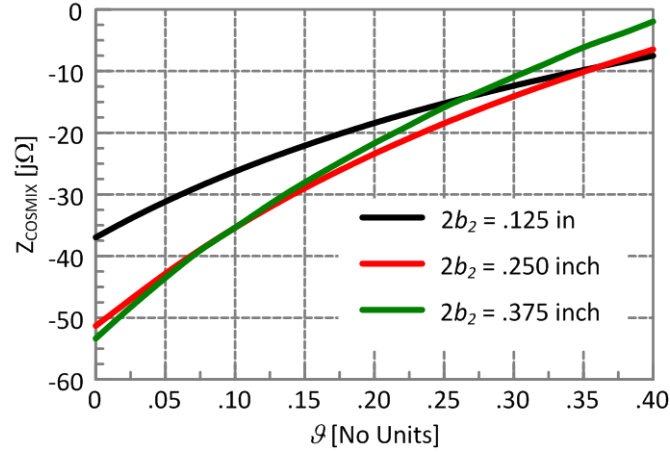
Fig. 49. Impedance of the COSMIX with different outer radii

Simulations then examined the RA element for its potential is respond to the impedance provided by the COSMIX (grey shadow in Fig. 50). Similar to the design process for the 2nd prototype, the COSMIX is replaced with a coaxial impedance port, and that port is moved away from the radiating edge by a distance s. Overlaying the windows from the COSMIX simulations shows that that reducing the COSMIX outer radius will hinder the phase response by providing less potential overlap with the phase curves. The placement of $s = 10$ mm provides a reasonable phase curve within the impedance window and will result in less peak attenuation compared to $s = 14$ mm.
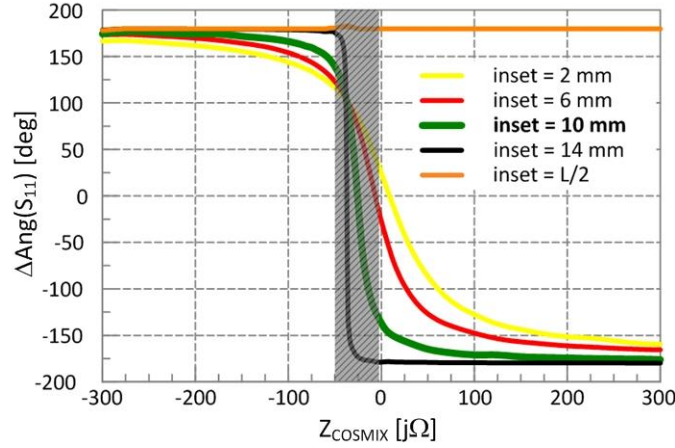
Fig. 50. Phase shift resulting from an impedance at the COSMIX interface

While the impedance window does not completely encompass the $s = 10$ mm phase curve, a simulation investigated just how much phase shift it could contribute in the current device. Fig. 51 shows CAD models representing two different methods for simulating the prototype RA unit cell. The model of Fig. 51, right uses periodic boundary conditions and a Floquet mode port. Simulating only the lowest order mode provides the scattering of a vertically polarized TEM plane wave incident upon an infinite array of unit cells. Fig. 52 compares the simulated results of this model with the waveguide simulation. The two simulation methods compare very well as established in [27]. Adjusting the volume fraction from 0% to 40% provides 310° of phase shift in the waveguide simulation and 280° in the TEM simulation. The greater field intensity in the center of the RWG (from the TE_{10} mode in the guide) will result in a greater interaction with the patch and less interaction with the peripheral area around the patch. This greater interaction in turn leads to more attenuation and more phase shift. When accounting a

high loss tangent in the fluid, tan δ_l, the peak RL is -10 dB, a value competitive with other works in the literature.
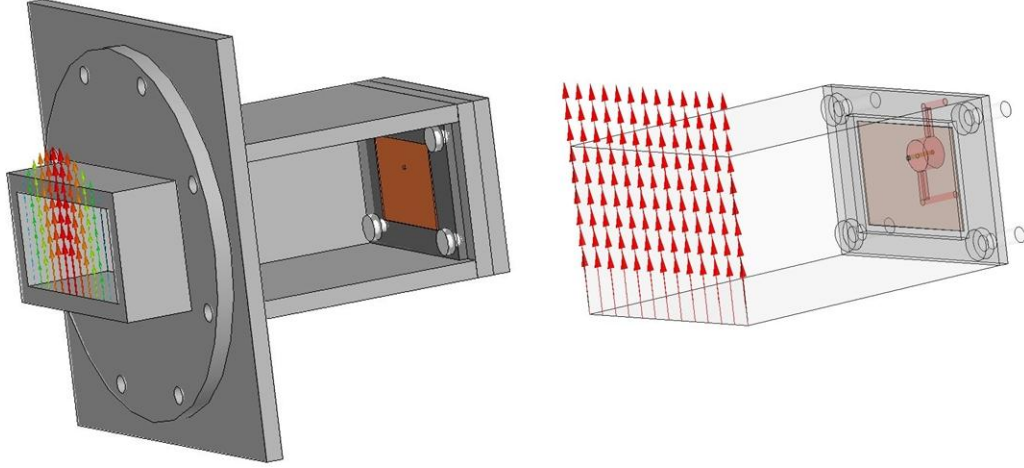
Fig. 51. Simulated model using a rectangular waveguide (left) and using a TEM plane

wave (right)
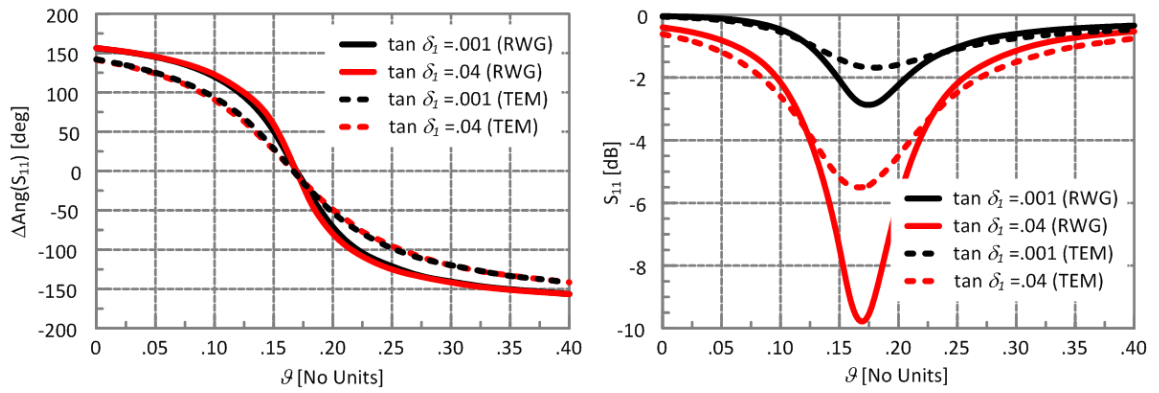
Fig. 52. Simulated phase shift (left) and return loss (right) of the third prototype

C. Experiment

The RA element and test fixture of Fig. 51 were fabricated in a similar manner to the second prototype. A test setup with only the measurement cell and no RA element was arrangement in a similar manner to Fig. 38. The experiment called for an initial high volume fraction of $\vartheta = 30\%$ and then dilution in 1% increments down to $\vartheta = 10\%$. This represents twice the range of the previous experiment which featured a COSMIX placed in a location providing greater phase sensitivity. Unfortunately the fluidic system experienced a catastrophic failure when the BSTO particles formed a clot in the syringe tip (Fig. 53), a subsequent pressure buildup, and finally a blowout. This cancelled further experimentation with the measurement cell and the 3rd RA prototype as both devices feature inlet radii designed to mate with the 15 (needle) gauge syringe tip. The RA element features an additional bottleneck for the material since its rectangular channels are exceptionally thin with $h_{ch} = 0.5$ mm.

Fig. 53. Clot formed in the blunt syringe tip

D. Contributions

This prototype goes beyond the considerations in earlier designs that focused on solely on operation of the RA element. This design accounts for factors external to the RA element including fabrication difficulties, implementation in an array environment, and the potential integration of other fluidic devices. The simulations highlight a design process geared toward other considerations aside from providing a steep phase curve. The simulated results examine both the fluidic and electromagnetic implications of adjusting the physical parameters of the COSMIX. The measurement (failure) highlights the need for the fluidic systems in future designs to expand channels for easier flow.

CHAPTER VII

FOURTH ITERATION

A. *Modifications*

Experiments with $\vartheta = 30\%$ with the third iteration failed due to material clotting in the blunt syringe. The fluidic network (Fig. 54) requires an expansion to $w_{ch} = 2\rho = 2.381$ mm (3/32 in.) to accommodate larger 14 gauge syringe tips. The inlet rectangular channel has been removed completely and the vertical feed now axially aligns with the COSMIX. This forces material displacement to occur in the capacitive gap and reduces the overall footprint of the fluidic network beneath the RA element. The height of the remaining vertical channel increases to $h_{ch} = 1.5$ mm.
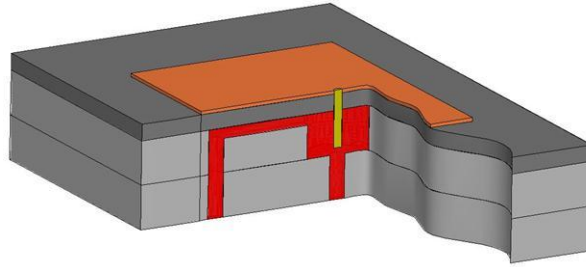
Fig. 54. Fourth iteration of RA element

The unit cell dimensions remain $(A_2, B_2) = (72.14$ mm, 50 mm$)$. A slightly thinner substrate ($h = 93$ mil) replaces the 125 mil substrate due to issues involving material availability in the lab. The new patch dimensions ($L = 31.5$ mm, $W = 38.7$ mm) reflect this change in substrate. The COSMIX position $s = 10$ mm and length $d = 6.35$ mm

remain unchanged from the previous iteration. Placing the COSMIX closer to center of the patch moves the outlet closer to edge of the unit cell boundary.

The primary motivation behind the design features of the fourth iteration RA element was the enhanced flow of the dispersions within the COSMIX. However, the placement of the inlet beneath the COSMIX provides a unique opportunity for enhancing the electrical performance as well. Fig. 55 illustrates that the probe can now insert into the inlet (i.e. negative value for *g*). This insertion transforms the basic model of the capacitive termination in the COSMIX.

Fig. 55. Insertion of the probe into the inlet

Fig. 56. New T-line representation of COSMIX

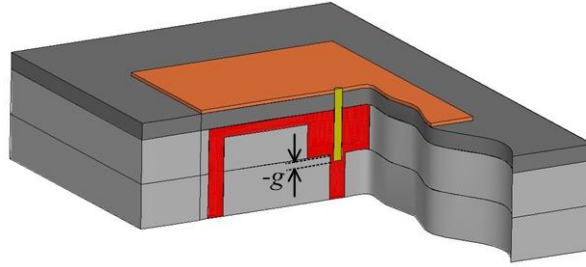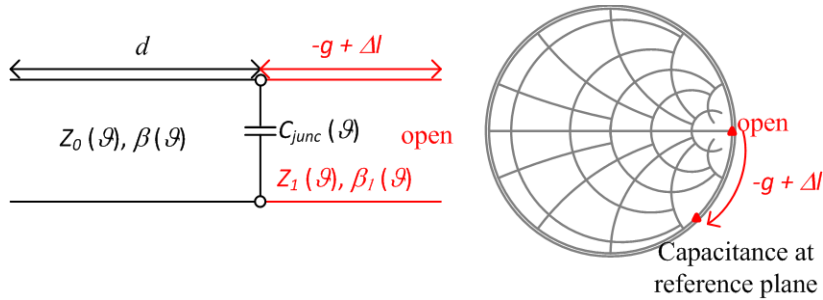Fig. 56 depicts how inserting the probe into the inlet transforms the capacitive gap into a capacitive junction between coaxial lines of different outer radii [23] followed by a length of transmission line followed by a termination into a circular waveguide in cutoff (an open circuit with a small length extension Δl). The open circuit in series with a small length of transmission line effectively represents as an additional capacitance at the reference plane of the junction. If the dielectric constant of the dispersion remains the same, then inserting the probe increases the net capacitance (Fig. 57) where the gap used to be. Or rather for the same capacitance a lower dielectric constant is required. Thus inserting the probe further in will shift the impedance curves (and phase curves) to lower volume fractions. The trade-off is potential material blockage due in the tight clearance between the probe and inlet. The potential harm here may be greater than the problem the fourth iteration was originally designed to mitigate.

$$d$$

$$Z_0(\vartheta),\ \beta(\vartheta) \qquad C_{junc}(\vartheta) + C_{inlet}(\vartheta)$$
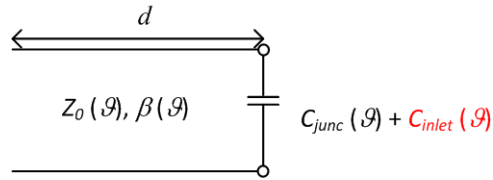
Fig. 57. Equivalent representation of COSMIX termination

B. Simulation

The simulated input impedance shown in Fig. 58 highlights the impact of the gap region on the performance of the COSMIX. Consistently inserting the probe into the feed shifts the impedance curves to lower volume fractions and may serve as a tuning mechanism.

Unlike all other physical parameters of the RA element and test fixture, the depth of the probe is easily adjusted after fabrication. The process consists of simply heating a solder connection between the patch and the probe and applying a small amount of pressure to lower the probe can incrementally move the probe down.

Fig. 58. Simulated input impedance of the COSMIX with different values of *g*

Fig. 59. Simulated phase shift (left) and return loss (right) of the fourth prototype

Fig. 59 shows how the shifts in input impedance translate to shifts in the scattering phase. A small adjustment of 1 mm in the probe depth can shift the phase and RL curves by as much as $\Delta\vartheta = .18$ and potentially compensate for inaccurate material data. These results highlight the potential of the probe position to profoundly alter the operation of the RA element.

C. Experiment

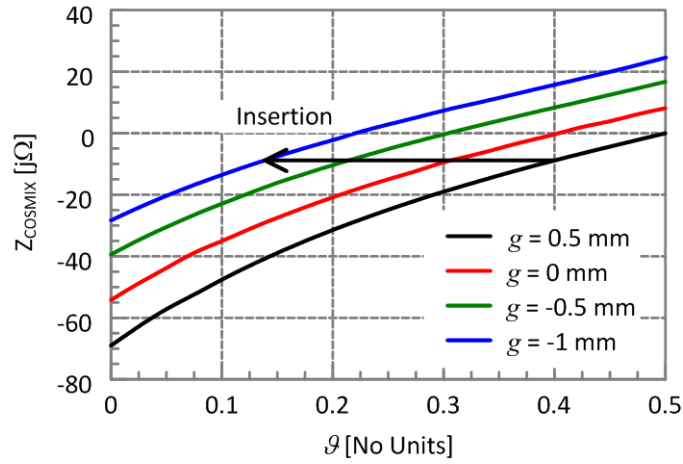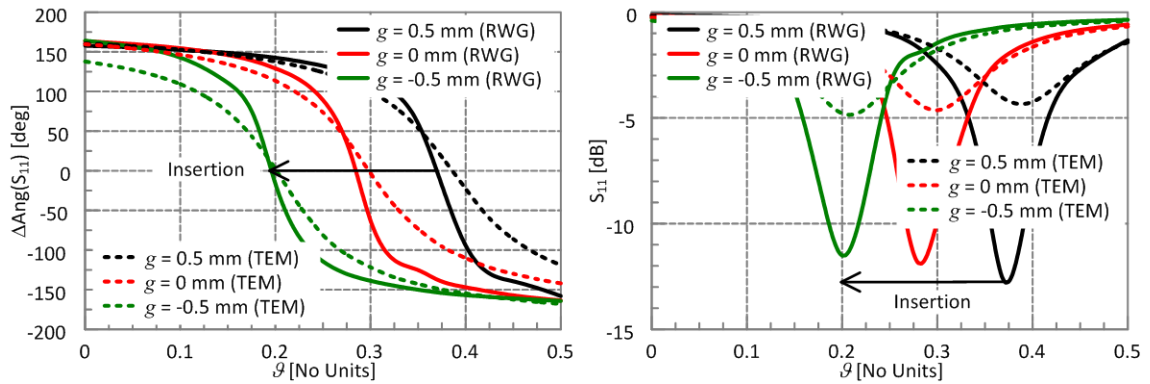Despite the possibility of phase shift at lower volume fractions, the gap dimension remains $g = 0.5$ mm to address the primary concern, clotting. The dimensions of this prototype allow for an experiment using the waveguide of the previous chapter, but a free-space measurement provides additional insight into the illumination and operation of the RA element. The measurement setup in Fig. 60 shows the RA element supported by a block of foam and illuminated by an S-band standard gain horn (SGH). A PNA connected to the SGH measures the signal reflected from the element back into the horn. The material delivery system in Fig. 60 (right) is identical to the previous experiment and flows dispersions to and from the COSMIX within the element to manipulate its reflection. Time-gating the measurement in the PNA attenuates interfering reflections from the lab environment but the material delivery system (i.e. the pump, the stirrer, the metal support structure) remains a persistent interferer because of its relative size and proximity to the element being observed.
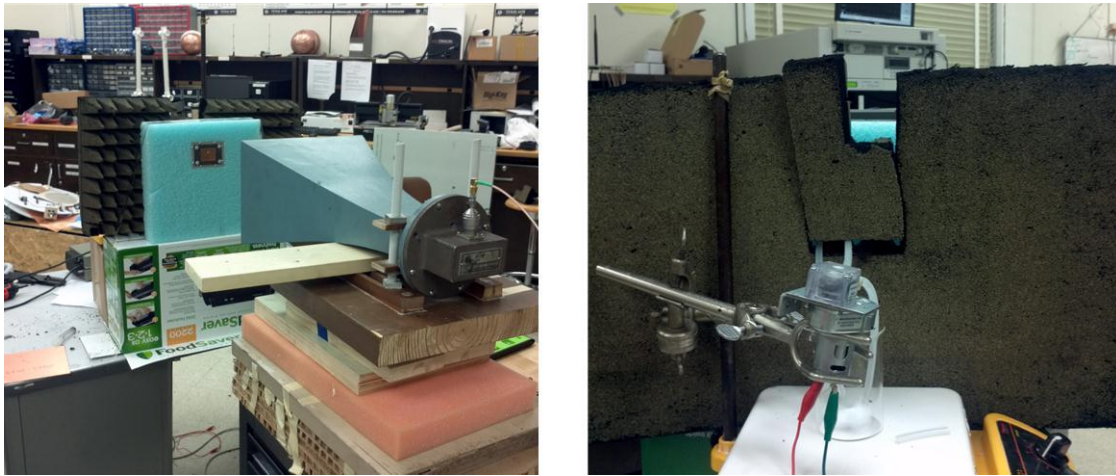
Fig. 60. Free-space reflection measurement of an isolated RA element (left) and material

delivery system (right)

A panel of absorbing material from an anechoic chamber shields the measurement from

this interference by dissipating incident EM waves before they can come in contact with

the material system. Fig. 61 shows screenshots from the PNA measurement of RL with

and without the absorber backing. The red trace represents an RA patch with no material

system present in its vicinity. The yellow curve of Fig. 61 (left) is the result of placing

the material system behind the foam block holding the patch. Placing the absorber panel

in between the patch and the material system results in the yellow curve of Fig. 61

(right). The agreement between the red and yellow curves indicates the material system

interferes very little with the RA measurement.

Fig. 61. Screenshots of the PNA measurement with (left) and without (right) the

absorber backing

Previous experiments with a dynamic material system began with a high volume fraction then proceeded by diluting the reservoir. Initial attempts at this method using 800 nm BSTO and low viscosity silicon oil mixed to a volume fraction of $\vartheta = 30\%$ resulted in the clots similar to experiments in the previous chapter despite the increased inner diameter of the syringe. Reversing the order of the experiment (i.e. starting with $\vartheta = 0$ and adding BSTO) and switching to 100 nm BSTO prevented the sudden clotting. The smaller nanoparticles likely have a lower dielectric constant, but their ability to flow justifies the likelihood of requiring a slightly higher volume fraction.
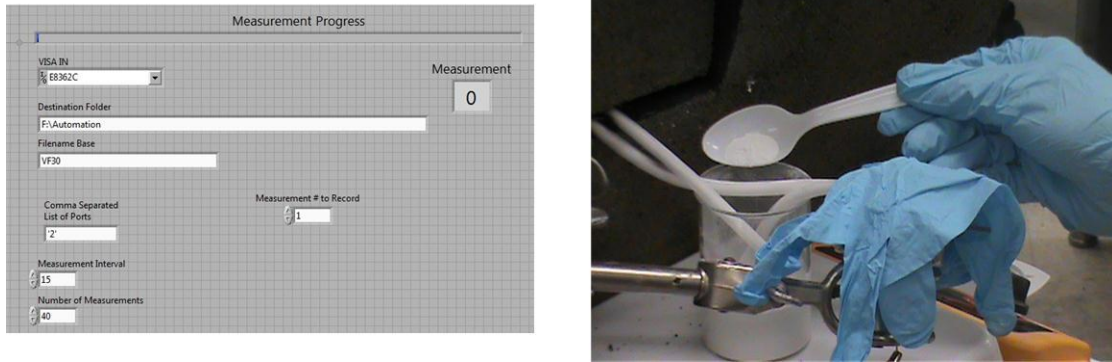
Fig. 62. A LabView GUI controlling the PNA (left) and incrementally adding BSTO to

raise the ϑ of the dispersion between measurement sets (right)

A LabView virtual instrument (Fig. 62, left) automated the measurement recording in

the PNA. The virtual instrument saved a measurement every 15 sec over a period of 10

minutes. After adding BSTO to the reservoir the cycle was reinitiated. The experiment

started with pure silicone oil ($\vartheta = 0$) and then 1g of BSTO was added to the system (Fig.

62, right) every measurement cycle until 32g were in the beaker. Then 2g were added

until 48g were in the beaker.

D. Results

Fig. 63 depicts measured phase curve at 3 GHz compared with simulated curves

representing various values of *g*. Early in the experiment, the phase decreases slightly

with every addition of material. However the rate of change never approaches what the

simulations suggest for $\vartheta > 20\%$. At a certain point the phase reverses direction and

increases.
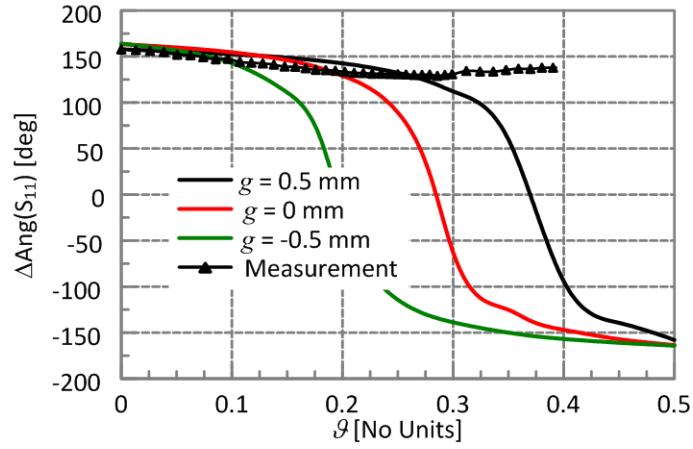
Fig. 63. Measured phase shift for the fourth RA prototype

More than halfway through the experiment the fluid exiting the RA was observed to be clearer than the material in the reservoir. The hypothesis is that the BSTO particles progressively formed a buildup within the COSMIX. Such a buildup would take nanoparticles out of circulation and lower the aggregate dielectric constant of the dispersion flowing through the capacitive gap. Ultimately this shifts the phase in the opposite direction. Disassembly of the RA element after the experiment confirmed this. The images of Fig. 64 show buildup occurred not only within the COSMIX within the reservoir a well.
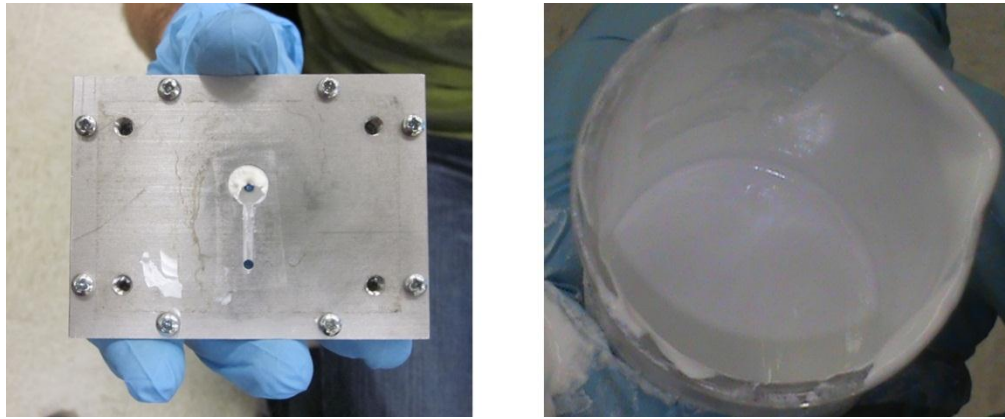
Fig. 64. Buildup of nanoparticles within COSMIX (left) and the reservoir (right)

E. Contributions

The fourth iteration improves the ability of the fluidic system to deliver material to the capacitive region of the COSMIX and reduces the footprint of the channels. In moving the inlet beneath the COSMIX a new degree of freedom may profoundly alter the phase performance for lower volume fractions. A new experiment method examines the performance of the RA element when illuminated by a SGH. The discovery of the nanoparticle buildup establishes a new goal for future designs.

CHAPTER VIII

MECHANISMS FOR FUTURE STUDY

A. *"Ductenna"*

Future reflectarrays developed from the unit cell topologies of this work will benefit from the use of a lightweight, low-cost, directional antenna for illumination. Open-ended waveguides such as the "cantenna" built from household items [21] satisfy many of these requirements, but tin cans fitting the proper dimensions for operation at 3 GHz or higher are elusive. Alternatively this work considers the use ductwork which is available in most home improvement stores and comes in a variety of diameters and lengths. Fig. 65 shows the model and fabricated "ductenna".
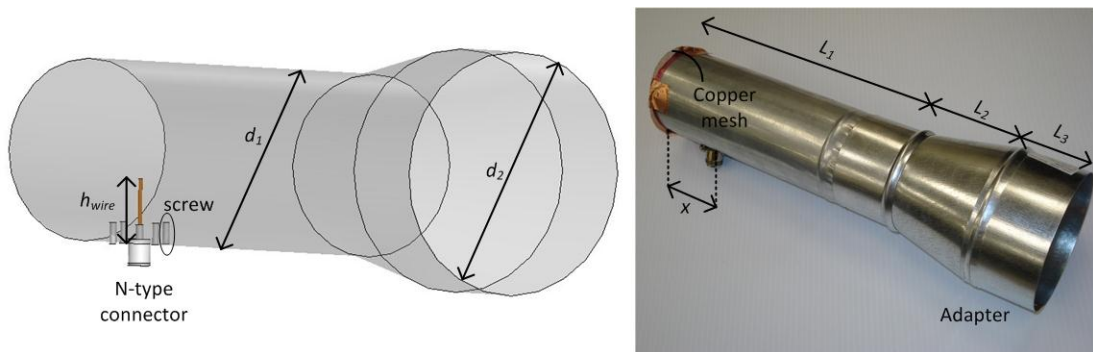
Fig. 65. Simulated model of the ductenna (left) and fabricated deign (right)

The design uses a section of ductwork with L_1 = 228.6 mm (9 in.) and d_1 = 76.2 mm (3 in.) connected to an adapter with L_2 = 69.85mm (2.75 in.), L_3 = 44.45 mm (1.75 in, and d_2 = 101.6 mm (4 in.). The adapter creates a larger aperture for increased gain. A N-type

connector mounts into the cylinder at $x = 42.96$ mm ($\sim\lambda_g/4$) from the back wall using a four-hole panel with steel screws that insert approximately 9 mm into the ductwork. A wire soldered to the connector inserts 25.4 mm (1 in.) into the antenna.
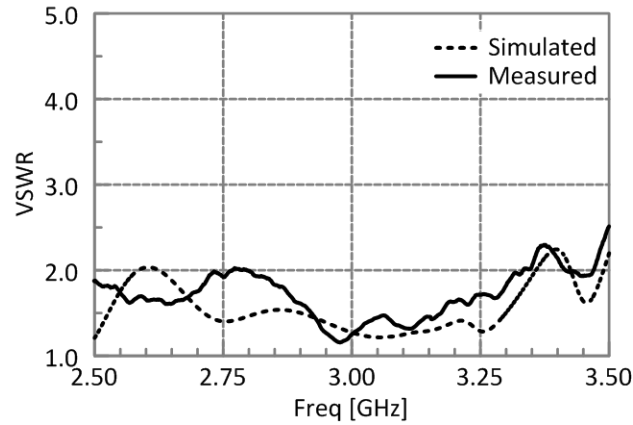
Fig. 66. VSWR of the ductenna

Fig. 66 shows the VSWR of the ductenna. The simulated and measured results agree very well and indicate the ductenna has a very large VSWR < 2 ($|S_{11}|$ < -10 dB) bandwidth. The simulated and measured radiation patterns in Fig. 67 also agree very well. The measured gain is 9.6 dB and the simulated gain is 10.3 dB. The simulations indicated a higher polarization purity than the measurement (i.e. only one color visible in each plot), but the cross-pol remains more than 10 dB weaker than the co-pol. This antenna will make a suitable feed for a wide range of RA sizes.
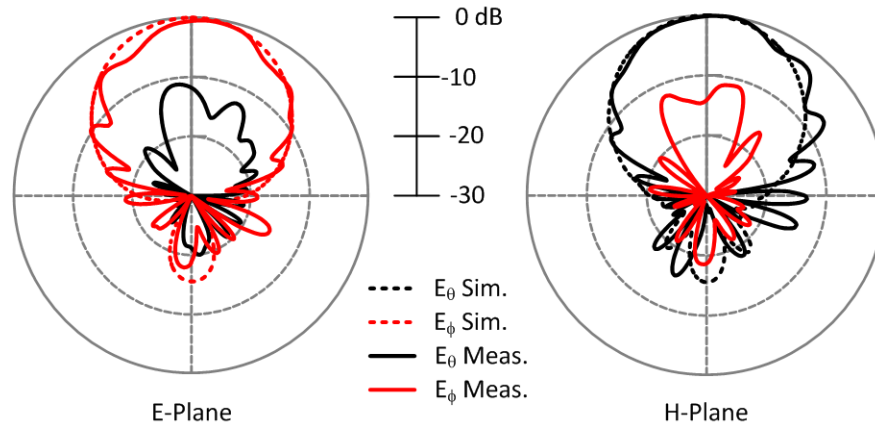
Fig. 67. Simulated and measured radiation patterns of the ductenna

B. *Pellets*

While constantly circulating fluidic systems capable of dynamic RA reconfiguration remain a consistent objective for future work, the presently available system shown in this work remains too large for every element in a large array to have its own. Operating an array of elements requires an alternative approach at this time. This work proposes the use of PDMS [35] loaded with BSTO and then cured into solid pellets in the shape of the COSMIX. Insertion of these pellets beneath RA elements provides a method of phase control similar to the manual injection method of the first prototype.
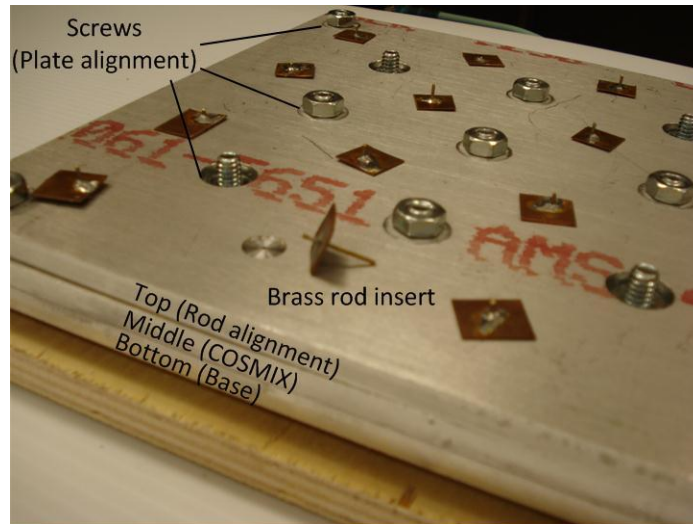
Fig. 68. Mold for forming COSMIX pellets

Fig. 68 shows a mold fabricated from three aluminum plates aligned and fastened together with screws. The bottom plate simply serves as a base while the middle plate features a 4 x 4 grid of $b_2 = 4.76$ mm holes. The top plates features $a_2 = 0.6$ mm holes through which brass rods of identical radius insert. The rods leave enough clearance to provide a section of material for the capacitive gap. The pellet "baking" process begins with securing the bottom and middle plates together and then placing them in a 70° C oven. While these plates heat up, the PDMS is prepared and the BSTO is added and mixed to provide a desired ϑ. When the dispersions are ready for pouring the plates are removed from the oven and the COSMIX sized holes are filled with the dispersion. The top plate is quickly secured and then rods the rods insert through the top plate. The assembled mold is placed back in the oven for an additional hour so accelerate the curing process of the PDMS. After removing the mold is removed from the oven and

disassembling it, the pellets are obtained. Fig. 69 shows pellets made from pure PDMS

and PDMS loaded with $\vartheta = 30\%$ BSTO.

Fig. 69. Pellets formed using pure PDMS (left) and BSTO-loaded PDMS (right)

C. 1 x 5 Array

Fig. 70 shows a fabricated 1 x 5 array based on the fourth iteration unit cell. Although

experiments with this unit cell suffered from nanoparticle buildup, the discovery and

availability of smaller nanoparticles with high dielectric constants as well as the

continued development of circulation systems may alleviate this problem. To that end

the array shown here can utilize those material systems in the future as well as the

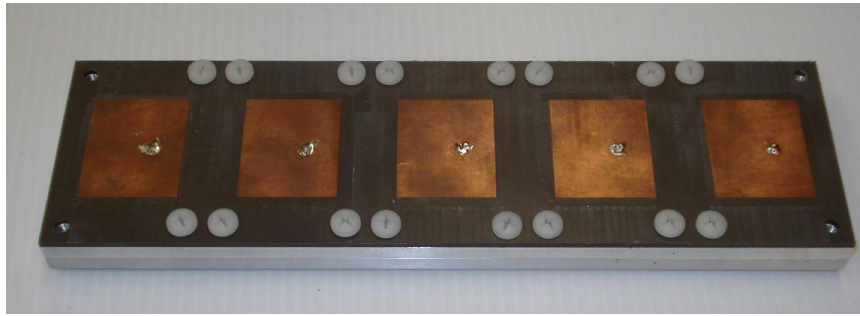aforementioned pellets for experiments in the present.

Fig. 70. Fabricated five element array

CHAPTER IX

CONCLUSION

This work has introduced and developed an original mechanism for manipulating the reflect-phase of an RA element. The bio-inspired approach utilizes a circulatory system to flow a dispersion of adjustable permittivity through a coaxial stub loading the element. This approach holds significant promise as a beam-forming topology due to its continuously tunable nature its ability to remove bias lines and control circuitry from the front end of the RA.

Theoretical models help to demonstrate the link between the adjustable composition of the dispersion and the shifted phase of a signal reflecting off an RA unit cell. Simulations and measurements prove this concept by placing the element in a waveguide and recording the phase shift as the material within the element is manipulated. The concept has been proven but its application continues to evolve through the several iterations within this work. The first prototype required disassembly and manual injection of premixed materials to achieve 200° of phase shift. The second prototype introduced the first ever circulatory system in an RA to replace this cumbersome process. Furthermore, this prototype introduced an intuitive design process led to enhance the performance of the loading mechanism. A successful measurement of 270° of phase shift validated this design process as well as the general principle of the fluid-tuned RA. The third prototype introduced a new fabrication method and channel layout

to provide a more functional RA element. The fluidic network was redesigned in the fourth and final literature in this work to not only flow material better, but also to potentially enhance the electromagnetic performance of the loading mechanism.

The topology of this work may continue to evolve to take advantage of new materials as they become available. Fluids with lower dielectric loss tangents will reduce the return loss of the element to an even more competitive value. Nanoparticles with higher permittivity and high aspect ratio geometries will reduce the volume fractions necessary to achieve reconfiguration of the RA phase. The RA unit cell loading mechanism of this work has demonstrated the potential to take advantage of many different materials in the future.

REFERENCES

[1]   J. Huang and J. A. Encinar, *Reflectarray Antennas*. Hoboken, NJ: Jogn Wiley & Sons, 2008.

[2]   A. Georgiadis, "Patents on reconfigurable reflectarray antennas," *Recent Patents on Electrical Engineering,* vol. 2, pp. 19-26, 2009.

[3]   A. E. Martynyuk, A. G. Martinez-Lopez, and J. Rodriguez-Cuevas, "Spiraphase-type element with optimal transformation of switch impedances," *Electronics Letters,* vol. 46, pp. 673-675, 2010.

[4]   O. Bayraktar, K. Topalli, M. Unlu, O. A. Civi, S. Demir, and T. Akin, "Beam switching reflectarray using RF MEMS technology," in *Proc. European Conference Antennas and Propag. (EuCAP 2007)*, Nov. 2007, pp. 1-6.

[5]   M. Sazegar, A. Giere, Z. Yuliang, H. Maune, A. Moessinger, and R. Jakoby, "Reconfigurable unit cell for reflectarray antenna based on barium-strontium-titanate thick-film ceramic," in *Proc. European Microwave Conference (EuMC 2009),* Sept. 2009, pp. 598-601.

[6]   R. Marin, A. Moessinger, F. Goelden, S. Mueller, and R. Jakoby, "77 GHz reconfigurable reflectarray with nematic liquid crystal," in *Proc. European Conf. Antennas and Propag. (EuCAP 2007)*, Nov. 2007, pp. 1-5.

[7]   A. Moessinger, R. Marin, S. Mueller, J. Freese, and R. Jakoby, "Electronically reconfigurable reflectarrays with nematic liquid crystals," *Electronics Letters,* vol. 42, pp. 899-900, 2006.

[8]   G. H. Huff, D. L. Rolando, P. Walters, and J. McDonald, "A frequency reconfigurable dielectric resonator antenna using colloidal dispersions," *IEEE Antennas and Wireless Propagation Letters,* vol. 9, pp. 288-290, 2010.

[9]   G. H. Huff, S. Goldberger, and S. A. Long, "The RF cuttlefish: Overview of biologically inspired concepts for reconfigurable antennas and smart skins," in *Proc. Antenna Applications Symposium*, Sept. 2008, vol. 31, pp. 57-62.

[10]   S. A. Long and G. H. Huff, "A substrate integrated fluidic compensation mechanism for deformable antennas," in *Proc. NASA/ESA Conf. Adaptive Hardware and Systems (AHS 2009).* July 2009, pp. 247-251.

[11]   O. Bayraktar, K. Topalli, M. Unlu, I. Istanbulluoglu, E. U. Temocin, H. I. Atasoy, O. A. Civi, S. Demir, S. Koc, and T. Akin, "Reconfigurable reflectarray

using RF MEMS technology," in *Proc. European Conf. on Antennas and Propag. (EuCAP 2006)*, 2006, pp. 1-4.

[12]   C. Chih-Chieh and A. Abbaspour-Tamijani, "Design and experimental verification of steerable reflect-arrays based on two-bit antenna-filter-antenna elements," in *Proc. Microwave Symposium Digest, 2009. MTT '09. IEEE MTT-S International*, June 2009, vol. 3, pp. 1181-1184.

[13]   H. Rajagopalan, Y. Rahmat-Samii, and W. A. Imbriale, "Reconfigurable patch-slot reflectarray elements using RF MEMS switches: a subreflector wavefront controller," in *Proc. IEEE Int. Symp. Antennas and Propag.*, June 2007, vol. 2 pp. 5203-5206.

[14]   H. Rajagopalan, Y. Rahmat-Samii, and W. A. Imbriale, "RF MEMS actuated reconfigurable reflectarray patch-slot element," *IEEE Transactions on Antennas and Propag.,* vol. 56, pp. 3689-3699, 2008.

[15]   B. Wu, A. Sutinjo, M. E. Potter, and M. Okoniewski, "On the selection of the number of bits to control a dynamic digital MEMS reflectarray," *IEEE Antennas and Wireless Propag. Letters,* vol. 7, pp. 183-186, 2008.

[16]   J. Perruisseau-Carrier and A. K. Skrivervik, "Monolithic MEMS-based reflectarray cell digitally reconfigurable over a 360 degree phase range," *IEEE Antennas and Wireless Propag. Letters,* vol. 7, pp. 138-141, 2008.

[17]   R. Marin, A. Mossinger, J. Freese, S. Muller, and R. Jakoby, "Basic investigations of 35 GHz reflectarrays and tunable unit-cells for beamsteering applications," in *Proc. European Radar Conference (EURAD 2005)*, Oct. 2005, pp. 291-294.

[18]   C. A. Balanis, *Antenna Theory: Analysis and Design*, 3rd ed. Hoboken, NJ: John Wiley & Sons, Inc, 2005.

[19]   W. L. Stutzman and G. A. Thiele, *Antenna Theory and Design*, 2nd ed. Hoboken, NJ: John Wiley & Sons, 1998.

[20]   A. Sihvola, *Electromagnetic Mixing Formulas and Applications* vol. 47. London: IEE, 1999.

[21]   A. Kumar, A. R. Madaria, and C. Zhou, "Growth of aligned single-crystalline rutile TiO2 nanowires on arbitrary substrates and their application in dye-sensitized solar cells," *The Journal of Physical Chemistry C,* vol. 114, pp. 7787-7792, 2010/05/06 2010.

[22]   D. M. Pozar, *Microwave Engineering*, 3rd ed. Hoboken, NJ: John Wiley & Sons, Inc., 2005.

[23]   N. Marcuvitz, *Waveguide Handbook*. London: Peter Peregrinus Ltd., 1986.

[24]   Ansoft, HFSS v12.0, Pittsburg, PA, 2009.

[25]   S. M. Shajedul Hasan, M. Sundaram, K. Yoon, and M. K. Howlader, "Measurement of dielectric properties of materials using transmission/reflection method with material filled transmission line," in *Proc. IEEE Instr. and Meas. Technology Conf. (IMTC 2005)*, May 2005, pp. 72-77.

[26]   F. Venneri, S. Costanzo, and G. Di Massa, "Transmission line analysis of aperture-coupled reflectarrays," *Progress In Electromagnetics Research,* vol. 4, pp. 1-12, 2008.

[27]   S. V. Hum, M. Okoniewski, and R. J. Davies, "Modeling and design of electronically tunable reflectarrays," *IEEE Trans. Antennas and Propag.,* vol. 55, pp. 2200-2210, 2007.

[28]   G. H. Huff and S. Goldberger, "A coaxial stub microfluidic impedance transformer (COSMIX)," in *IEEE Microwave and Wireless Components Letters,* vol. 20, pp. 154-156, 2010.

[29]   TPL Inc., NanOxide HBS-8000, Albuquerque, NM, 2006.

[30]   Spectrum, SI114 Silicone Fluid, Gardena, CA, 2011.

[31]   Agilent Technologies, 85070E Dielectric Probe Kit, Santa Clara, CA, 2011.

[32]   Agilent Technologies, E8361C PNA Network Analyzer, Santa Clara, CA, 2011.

[33]   B. Li, X. Wang, L. Li, H. Zhou, and X. Liu, "Dielectric properties of fine-grained BaTiO3 prepared by spark-plasma-sintering," *Materials Chemistry and Physics,* vol. 83, pp. 23-28, 2004.

[34]   COMSOL Group, COMSOL Multiphysics, Stockholm, Sweden, 2011.

[35]   Dow Cowrning, Sylgard 184, Midland, MI, 2011.

VITA

Stephen Andrew Long was born in Houston, TX. He has attended Texas A&M University since 2002 and received his B.S. and M.S. degrees in 2006 and 2009, respectively, and he has recently completed his Ph.D in 2011. He is a student member in both IEEE and IET. His research has examined reconfigurable antennas and other dynamic hardware. His most recent focus has been on the use of fluidic networks to achieve reconfiguration typically provided by more conventional electronics.

He is currently employed at Electrical and Computer Engineering Department at Texas A&M as a graduate researcher and at the U.S. Naval Research Lab as an intern engineer. While at A&M he has presented his work at several conferences and competitions. His work on compensation for deformable antennas won the Best Paper in Reconfigurable Hardware in 2009. He was the runner-up in the student paper competition at the Antenna Applications Symposium in 2010 for his doctoral research. He was also the runner-up in the Americas regional for the IET's Present Around the World competition in 2011.

Stephen Andrew Long may be reached at 323 Zachry Engr Bldg., Texas A&M University, College Station, TX 77843-3128. His email is friendlyaggie@gmail.com.